JOURNAL OF GEOPHYSICAL RESEARCH, VOL. 105, NO. C7, PAGES 16,857–16,883, JULY 15, 2000

Thermohaline variability in the upper ocean

Raffaele Ferrari and Daniel L. Rudnick
Scripps Institution of Oceanography, La Jolla, California

Abstract. The main goal of this exploratory study is to determine how the temperature-salinity relationship changes with horizontal length scale and depth in the ocean. Temperature and salinity were measured on a range of scales from 4 m to 1000 km, towing a SeaSoar along isobars and isopycnals in the subtropical gyre of the North Pacific, during the winter of 1997. The wavelet transform technique is used to compute the horizontal density ratio and thermohaline variability as a function of scale and location. Measurements along an isobar in the mixed layer show that the horizontal density ratio is 1 at all scales observed; that is, horizontal temperature and salinity gradients tend to cancel each other in their effect on density. Thermohaline variability at small scales is intermittent and clusters around large-scale thermohaline anomalies. Below the base of the mixed layer, horizontal gradients of temperature are only partially opposed by salinity, and the density ratio is close to 2. In the thermocline the distribution of thermohaline variability is uniform along isobars but intermittent and colocated at different scales along isopycnals. Density-compensated variability, ubiquitous in the mixed layer, is reduced along deeper isopycnals. Compensation of horizontal temperature and salinity gradients supports recent theoretical ideas that mixing in the winter mixed layer depends on horizontal density gradients.

1. Introduction

In the upper ocean, a remarkable correlation exists between temperature and salinity gradients. In the mixed layer, abundant examples of horizontal fronts with temperature and salinity that nearly cancel in their joint effect on density can be found on scales of 10-100 km [i.e., *Roden*, 1975, 1989; *Yuan and Talley*, 1992). A few observations have been made of horizontal density fronts on scales finer than 10 km in which the temperature gradient is partially opposed by the salinity gradient [e.g., *Flament et al.*, 1985; *Rudnick and Luyten*, 1996]. A useful measure of the degree of compensation is the density ratio R defined as the ratio of the relative effect of temperature and salinity on density over a spatial interval. A front that is cold and fresh on one side and warm and salty on the other, so that temperature and salinity have opposing effects on density, has a density ratio of 1. A front where the effect of temperature is twice and opposite to that of salinity has a density ratio of 2. *Stommel* [1993] and *Chen* [1995] computed the density ratios of large-scale meridional temperature-salinity (T-S) gradients in the surface waters of all oceans in the range of latitudes between 20° and 50° and concluded that R has a mean close to 2, even though individual fronts can have a density ratio markedly different from 2. On smaller horizontal scales, between 20 m and 10 km, *Rudnick and Ferrari* [1999] found that the mixed layer density ratio is 1, not 2. In the waters just below the subtropical mixed layer, density variations due to temperature are often opposed by those due to salinity. Density ratios computed across vertical distances of 1-10 m are typically between 2 and 3 [e.g., *Schmitt and Evans*, 1978; *Dugan et al.*, 1992; *Mack and Schoeberlein*, 1993]. A first goal of this exploratory study is to determine how the density ratio changes with spatial scale and vertical position in the upper 300 m of the subtropical oceans.

The establishment of T-S compensation in the mixed layer can be rationalized in a few different ways. One explanation is that climatological distributions of precipitation, evaporation and air-sea heat exchange conspire with entrainment of thermocline waters to create and juxtapose patterns of temperature and salinity with a fixed density ratio. A more satisfactory explanation relies on regulating mechanisms in the mixed layer to create correlations between temperature and salinity, regardless of the large-scale atmospheric forcing. The basic idea is straightforward: temperature and salinity are dynamically active because they contribute to density gradients. All processes that depend on density gradients are potentially capable of creating T-S relations by acting only on fluctuations of temperature and salinity that reinforce in their joint effect on density. Perhaps the oldest branch of models in which the dynamics depends exclusively on horizontal density gra-

Paper number 2000JC900057.
0148-0227/00/2000JC900057$09.00

dients descends from *Stommel*'s [1961] two-box idealization of the thermohaline circulation. Stommel posited a transport law in which the exchange of mass between boxes is proportional to the square of the density difference. Some 30 years later, *Stommel* [1993] and *Stommel and Young* [1993] used the same model to propose a regulator mechanism for the mixed layer. The temperature and salinity in the two boxes are established by the interaction between a mean horizontal temperature gradient and a stochastic forcing of random rainfall and evaporation. Provided that the random fluctuations are large, the average ratio of the temperature and salinity differences across the two boxes is 2. A second class of models has been developed to parameterize the transport of heat and salt in a mixed layer idealized as a shallow system with strong vertical mixing. *Young* [1994] suggested that the horizontal diffusivity of temperature and salinity in such a mixed layer is proportional to the horizontal density gradient squared. The physical explanation of this parameterization is illustrated in the analysis of *Ferrari and Young* [1997]. Assume that atmospheric forcing and entrainment of thermocline waters create random distributions of temperature and salinity in the mixed layer. Regions will exist in which the horizontal gradients of temperature and salinity will happen to compensate in their effect on density, whereas in other regions they will create horizontal density gradients. The horizontal density gradients will slump under the action of gravity and restratify the mixed layer. Any subsequent strong vertical mixing results in a weakening of the horizontal density gradient. Those T-S gradients that are compensated do not slump and do not experience horizontal dispersion and therefore persist. The strength of the dispersion increases as the horizontal density gradient becomes larger and may be described by a horizontal diffusivity that is an increasing function of the density gradient. The specific functional dependence is determined by the details of the slumping process. At small horizontal scales this mechanism is essentially a shear dispersion driven by slumping horizontal density gradients, and the eddy diffusivity turns out to be proportional to the density gradient squared. At scales larger than the local Rossby radius, rotation affects the slumping in the form of baroclinic instability. The results of numerical simulations [*Pavan and Held,* 1996] and theoretical investigations [*Visbeck et al.,* 1997; *Haine and Marshall,* 1998] suggest the adoption of an eddy diffusivity proportional to a power of the horizontal buoyancy gradient between 1 and 3.

A tight relationship between temperature and salinity is also observed in the waters below the mixed layer. This has been described as the result of different processes. *Iselin* [1939] noticed that there is a correspondence between horizontal profiles in the surface mixed layer and vertical profiles in the upper thermocline. He concluded that water properties set in the winter mixed layer are transported to the interior essentially unchanged along surfaces of constant density. An alternative explanation is that the thermocline structure is established by double–diffusive mixing [*Schmitt,* 1981, 1999]. Salt fingers transport more salt than heat and tend to rotate and tighten the T-S curve. Further, salt finger convection is a strong function of the density ratio, decreasing rapidly for values larger than 2. Thus salt fingers can account for a tight T-S relationship and a density ratio of 2.

This study presents observations of the T-S relationship in the mixed layer and in the upper thermocline on an unprecedented range of horizontal scales from 10 m to 1000 km. T-S measurements were collected with a SeaSoar equipped with a conductivity-temperature-depth profiler (CTD). The development of a new vehicle control system to track isobars and isopycnals has been a key element in the success of the experiment. Data are analyzed using wavelet techniques to identify the distribution of T-S variability as a function of length scale and location. The wavelet transform [*Daubechies,* 1992] is a mathematical tool, much like the Fourier transform, of potential use in the analysis of data. In this paper, wavelet coefficients are used to calculate statistics relevant to thermohaline variability.

The paper is organized as follows. A summary of the data is given in section 2. Measurements along a surface of constant pressure in the mixed layer are used to discuss statistics of the density ratio and the distribution of thermohaline variability at different scales in section 3. The analysis of thermohaline variability is extended to measurements along isobars and isopycnals in the upper thermocline in section 4. Sawtooth profiles between the surface and 320 m are used to provide a description of the changes of thermohaline variability with depth in section 5. A summary and conclusions are provided in section 6.

2. Data

The Spice experiment consisted of a cruise in the eastern North Pacific along 140°W, between 25° and 35°N. This area is representative of the T-S variability of the North Pacific subtropical gyre, away from boundary currents. The cruise was conducted from January 24 to February 20, 1997. There were two main reasons to prefer wintertime for this experiment. First, the mixed layer is deep ($\sim$100 m) and well mixed so that the effects of diurnal solar heating are reduced. Second, the water found in the subtropical mixed layer in this season is subducted in the thermocline and plays an important role in the formation of central water masses.

Measurements were taken towing a SeaSoar equipped with a Sea-Bird CTD. All sensors were fixed to the rear wing of the SeaSoar pointing directly into the flow; their calibration is discussed in Appendix A. Upper bounds on instrumental errors, estimated as the RMS difference between the measurements returned by the two sets of sensors, are 1.3×10^{-3} °C for temperature, 1.4×10^{-3} psu

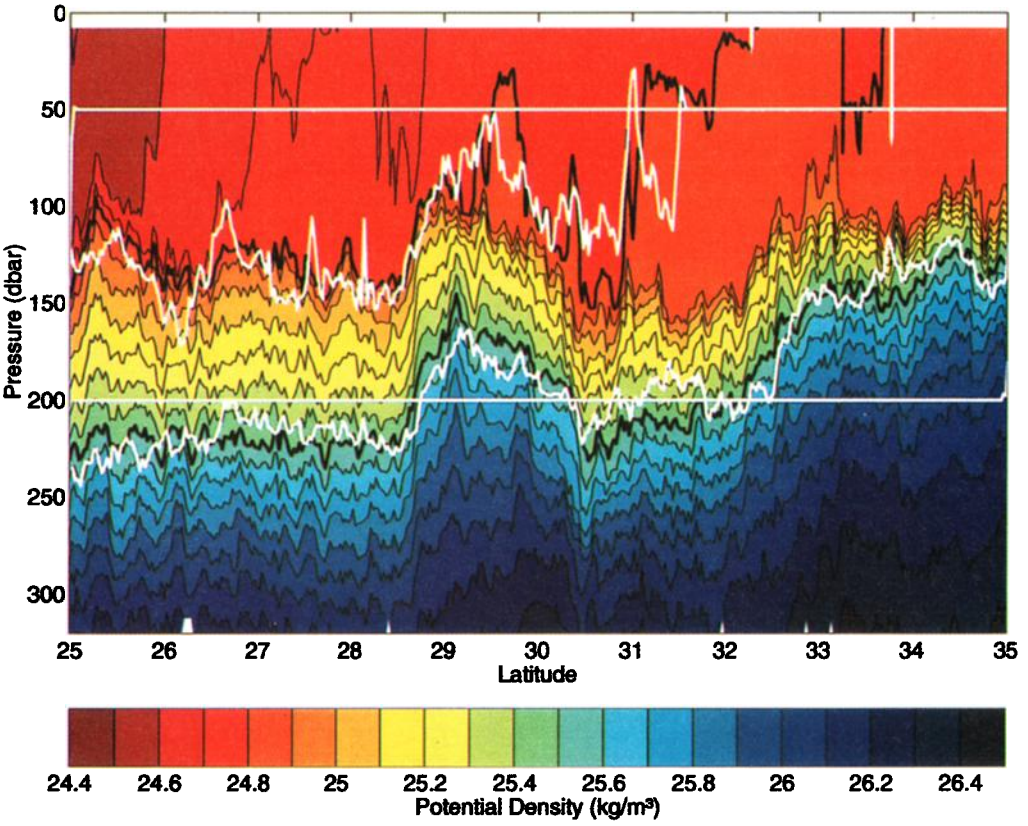

Plate 1. A summary of the Spice experiment data set. The potential density section along 140°W is measured towing a SeaSoar along a sawtooth path. The straight white lines are isobar tows at 50 and 200 dbar. The heavy black lines are isopycnals 24.8 kg m^{-3} and 25.5 kg m^{-3} as measured during the sawtooth tow. The jagged white lines are tows along these isopycnals.

for salinity, and 1.2×10^{-3} kg m^{-3} for potential density. Supporting measurements included a fluorometer, mounted on top of the SeaSoar body, Global Positioning System (GPS) navigation, a shipboard acoustic Doppler current profiler (ADCP), and meteorology.

The observational program consisted of five north-south sections of 10 degrees of latitude, approximately equivalent to 1100 km, in which the SeaSoar was towed along different measurable surfaces using a new digital flight controller. In the first section the SeaSoar was flown along a sawtooth profile. The controller commanded the SeaSoar to fly between 5 and 320 dbar in less than 12 min, while keeping dive rate and cable tension within specified bounds. The second and third sections were level tows at 50 dbar in the mixed layer and 200 dbar in the seasonal thermocline. The controller used the difference between the locally measured pressure and the pressure it was supposed to track to maintain the SeaSoar along the desired isobar. Surfaces of constant potential density were chosen for the last two sections, one that went from beneath the mixed layer to outcropping (24.8 kg m^{-3}) and the other that remained in the seasonal thermocline (25.5 kg m^{-3}). The controller operated by responding to differences between the chosen potential density and the one measured in real time. The isobar and isopycnal tow patterns were accomplished using a proportional integral derivative (PID) control algorithm [*Shinskey*, 1988].

A complete summary of the experiment is given in Plate 1. The potential density section, as measured by the sawtooth tow, provides the background thermohaline fields on scales larger than 3 km. At a cruising speed of $\sim$4 m s^{-1}, the SeaSoar completed a minimum of five and an average of seven cycles per hour. These data were averaged into bins of 12 min in time (a horizontal resolution of $\sim$3 km) by 8 m in depth. The length of the bins ensured that the SeaSoar completed at least one cycle per bin, while vertical resolution was set to be equal to the vertical resolution of the ADCP. This snapshot shows the main features of the upper ocean structure found in the survey region. There is a well developed mixed layer in the upper 100-150 m that sits over the thermocline. The corresponding pictures of potential temperature and salinity show that temperature is the vertically stratifying component, while salinity decreases with depth for latitudes south of 32°N.

High horizontal resolution was obtained by towing the SeaSoar along two isobars for the full 10° of latitude. The straight white lines in Plate 1 are isobar tows at 50 dbar in the mixed layer and 200 dbar in the

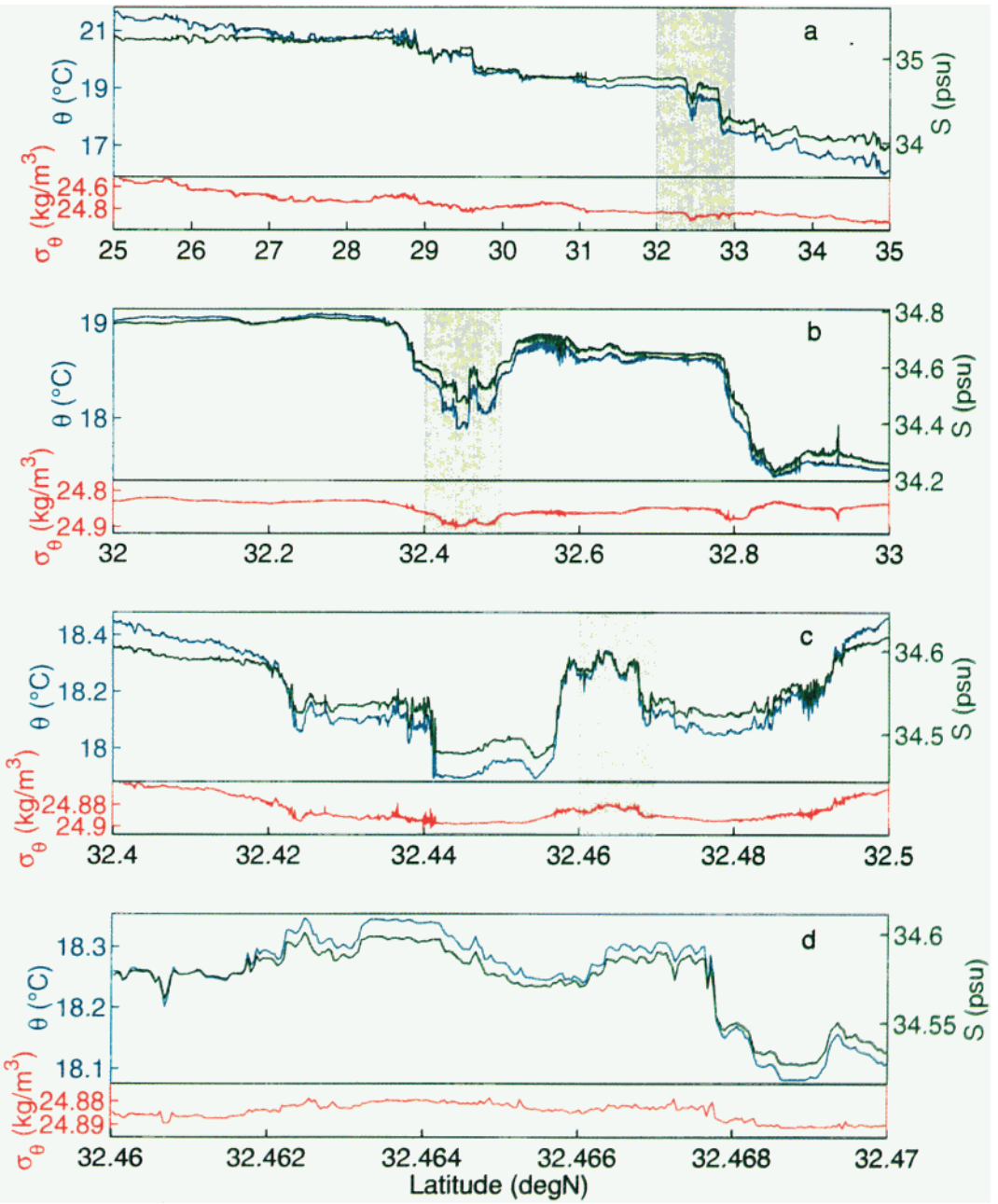

Plate 2. Potential temperature θ (blue lines), salinity S (green lines), and potential density σ_θ (red lines) along the 50 dbar pressure surface: (a) the signals over the entire tow from 25° to 35°N and (b), (c) and (d) successive magnifications by a factor of 10 of the shaded portion of the panel above. Plates 2a-2d span horizontal sections of 1113, 111, 11, and 1 km, respectively. The vertical axes for temperature and salinity are scaled by the thermal and haline expansion coefficients so that excursions of temperature and salinity are presented as the change they imply on density. Every temperature fluctuation is mirrored by one in salinity of the same amplitude that cancels its effect on density, even at the smallest scales.

seasonal thermocline. Stable temperature and salinity measurements were possible at a frequency of 1 Hz, and thus the isobar tows allowed a horizontal resolution of 4 m at a mean towing speed of 4 m s^{-1}. RMS speed fluctuations remained within 0.2 m s^{-1} and contributed to an uncertainty of 5% in estimates of spatial scales from temporal measurements. The control system worked better than anticipated, and the SeaSoar followed an isobar to within an RMS deviation of 0.3 dbar at an average slant of 0.4° in the mixed layer and an RMS of 0.4 dbar at an average slant of 1.0° in the thermocline.

The jagged white lines in Plate 1 are tows along isopycnals. The shallower tow tracked the isopycnal 24.8 kg m^{-3} starting from beneath the mixed layer and crossing its base south of 29°N, while the deeper tow followed an isopycnal in the upper thermocline (25.5 kg m^{-3}). The control system was successful at following isopycnals to within an RMS deviation of 0.02 kg m^{-3}. The black lines are the isopycnals 24.8 and 25.5 kg m^{-3} as measured during the sawtooth tow. The difference between the black and white lines is due to oceanic variability; that is, the isopycnals moved during the time between surveys.

3. Thermohaline Gradients in the Mixed Layer

The goal of this section is to obtain statistics of temperature and salinity fluctuations in the mixed layer along a horizontal surface. Horizontal scales below 1 km are poorly explored in the ocean, and simultaneous measurements of temperature and salinity in the mixed layer over a range of scales from 4 m to 1100 km are unprecedented to our knowledge. The measurements were made along the 50 dbar pressure surface, chosen to bisect roughly the mixed layer (Plate 1). These data are used in the following two sections (1) to quantify the degree of compensation between temperature and salinity over horizontal scales from 20 m to 10 km and (2) to show that frontal zones are composed of thermohaline fluctuations on a wide range of scales.

3.1. Thermohaline Compensation in the Mixed Layer

Data from the 50 dbar tow show that each feature in potential temperature is mirrored in salinity throughout the mixed layer over length scales from hundreds of kilometers down to several meters (Plate 2). Potential temperature and salinity gradients coincide so that density gradients are minimized: horizontal fronts tend to be cold and fresh on one side and warm and salty on the other. In Plate 2 the vertical axes for temperature and salinity are scaled by the corresponding expansion coefficients, so that a unit distance is the same in potential temperature, salinity, and potential density. This presentation emphasizes that temperature and salinity fluctuations have hardly any signature in density. Successive enlargements of a frontal region show that compensation occurs down to scales as small as 10 m. Strong horizontal density gradients are rarely observed at all scales. Pressure fluctuations around the depth of 50 dbar are small, with an RMS of 0.3 dbar, and not correlated with the thermohaline fields (Figure 1), proving that the observed gradients are not due to profiling vertical stratification.

The correlation between thermohaline gradients is often quantified in terms of the ratio of the relative effect of potential temperature and salinity on density, the density ratio,

$$R \equiv \frac{\alpha \Delta\theta}{\beta \Delta S}, \tag{1}$$

where $\alpha = -\partial\sigma_\theta/\partial\theta$ and $\beta = \partial\sigma_\theta/\partial S$ are the expansion coefficients of potential temperature and salinity in units of kg m^{-3} $°C^{-1}$ and kg m^{-3} $(psu)^{-1}$. The potential temperature and salinity differences $\Delta\theta$ and ΔS are taken over a spatial interval. Horizontal fronts in which temperature and salinity have opposing effects on density, as those shown in Plate 2, are said to be compensated and have a density ratio of 1. Fronts where the effect of temperature on density is larger and opposite to that of salinity have a density ratio between 1 and ∞. The arctangent of the density ratio is known as the Turner angle,

$$Tu = \arctan(R). \tag{2}$$

The branch of the arctangent is chosen such that $-\pi/2 < Tu \leq \pi/2$ (this choice differs from the one used in the literature on double diffusion but is more convenient for the present study). The Turner angle is positive when temperature and salinity counteract each other in their effect on density. Across compensated fronts, $\alpha\Delta\theta = \beta\Delta S$ and $Tu = \pi/4$, while temperature fronts only partially opposed by salinity have a Turner angle between $\pi/4$ and $\pi/2$. The advantages of using Tu rather than R are apparent: (1) the infinite scale of R is replaced by a finite one running from $-\pi/2$ to $\pi/2$, (2) the indeterminate value obtained when $\Delta S = 0$ is well defined in terms of Tu, and (3) temperature-dominated regions ($1 < R < \infty$) and salinity-dominated regions ($0 < R < 1$) occupy the same space on the Tu scale. All computations are therefore carried out in terms of Tu, but the results are discussed in terms of R because it has a more intuitive interpretation.

A quantitative description of the compensation seen graphically in Plate 2 is obtained by computing the density ratio over a wide range of horizontal scales. In order to determine temperature and salinity fluctuations as a function of scale and location the T and S signals are convolved with analyzing functions compact in location and wavenumber. Like a microscope, these functions increase spatial resolution to focus on progressively smaller scales at the cost of resolution in wavenumber. In fact, achieving arbitrarily high resolution both in location and wavenumber is impossible, in exact analogy with the Heisenberg uncertainty principle. A good compromise is obtained with a basis of

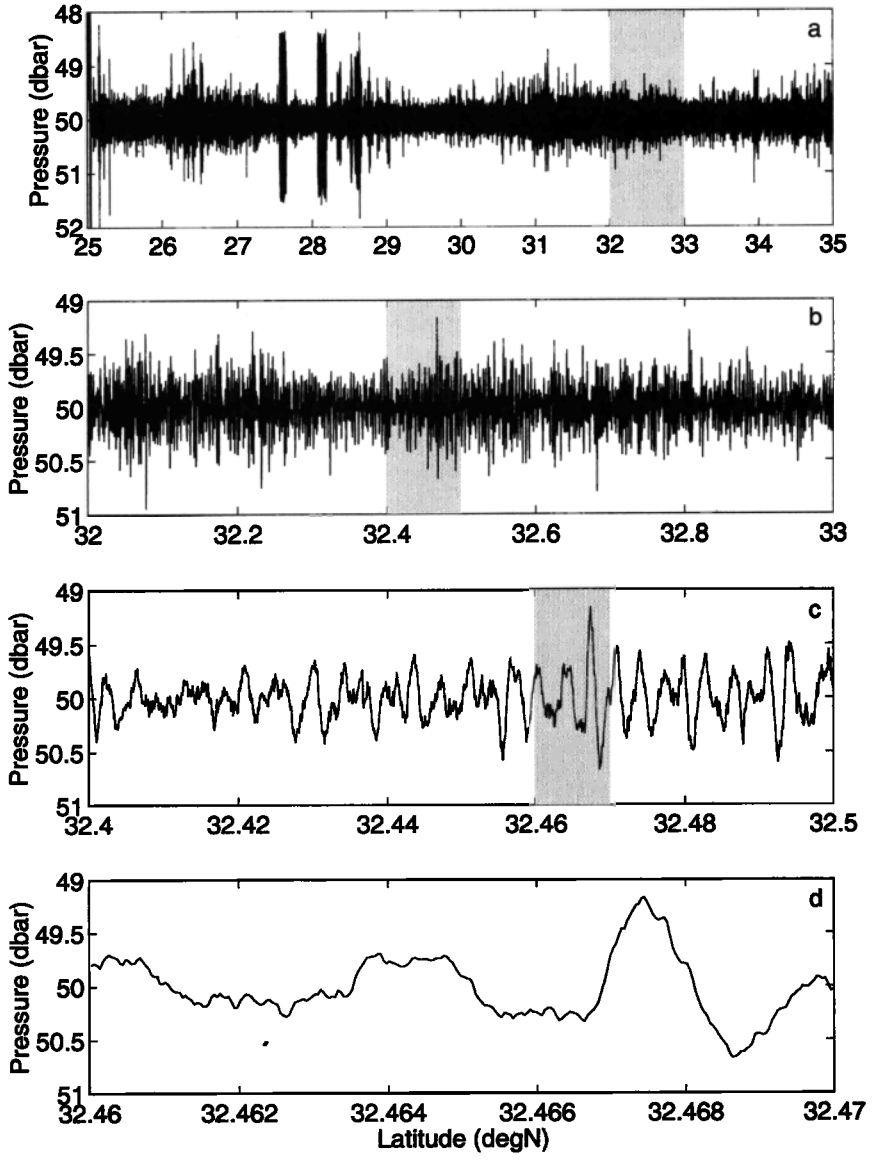

Figure 1. Pressure fluctuations measured by the SeaSoar during the isobar tow at 50 dbar. Figures 1a-1d show sections of the tow corresponding to the thermohaline measurements of Plates 2a-2d. Pressure is not correlated with the thermohaline fields, proving that the signals in Plate 2 are not due to profiling vertical stratification but reflect true horizontal variability.

analyzing functions in the form of wave packets localized in both spaces. By changing the wavelength of the oscillations proportionally to the e-folding of the wave packet in space the analyzing functions maintain a constant number of oscillations at all scales. This technique is generally referred to as the wavelet transform.

The wavelet transform is defined as the convolution of a signal with a set of functions, called wavelets, of changing width to resolve different scales (Appendix B). Wavelets are derived by dilation of the so-called mother wavelet, keeping constant the quality factor Q, defined as the ratio of the wavenumber at which the window is centered to its spread in wavenumber. In the following analysis the mother wavelet is a sinusoid multiplied by a Gaussian,

$$\psi(x) = \frac{1}{\sqrt{\pi}} \exp(-x^2) \exp(iQx),$$

with $Q = 2\sqrt{2}\pi$. This mother wavelet, generally referred to as the Morlet wavelet, is optimum in the sense that the product of the resolution in wavenumber with that in location is minimum in Hilbert space. The wavelet coefficients at scale l and position x_0 for potential temperature and salinity are given by

$$\Delta\theta(l, x_0) = \frac{1}{|l|} \int_{-\infty}^{+\infty} \psi^* \left(\frac{x - x_0}{l} \right) \theta(x) \mathrm{d}x \qquad (3)$$

$$\Delta S(l, x_0) = \frac{1}{|l|} \int_{-\infty}^{+\infty} \psi^* \left(\frac{x - x_0}{l} \right) S(x) \mathrm{d}x. \qquad (4)$$

The wavelet transform is here defined to have unit

gain so that the wavelet coefficients of a monochromatic signal of unit amplitude have unit amplitude at the wavelength of the monochromatic signal. The wavelet coefficients of θ and S are multiplied by the respective expansion coefficients α and β low passed at scales larger than l with a Gaussian filter $G_l(x) = 1/(\sqrt{\pi}\,|l|)\exp\left(-x^2/l^2\right)$. The resulting series $\alpha\Delta\theta(l, x_0)$ and $\beta\Delta S(l, x_0)$ give the amplitude and phase of temperature and salinity fluctuations in density units as a function of wavelength and location.

The real parts of the wavelet coefficients of potential temperature and salinity $\alpha\Delta\theta$ and $\beta\Delta S$, for horizontal wavelengths between 20 m and 10 km, are used to obtain a statistical description of thermohaline compensation. The wavelet coefficients by themselves are not a statistical measure; they are the result of a mathematical transform such as the coefficients of a Fourier transform. Compensation can be quantified only by computing statistics of the wavelet coefficients. Plate 3 displays the joint probability density functions (PDFs) of $\alpha\Delta\theta$ and $\beta\Delta S$ for wavelengths of 20 m, 100 m, 1 km, and 10 km. Thermohaline fluctuations tend to be larger at long wavelengths: the amplitude of the wavelet coefficients decreases by a factor of 4 between 10 km and 20 m. The joint PDFs have broad tails and peaked centers. Compensation is nearly total for the strongest fronts: these are the extreme events that extend out in the tails along the compensation line $\alpha\Delta\theta = \beta\Delta S$. At small scales the clouds of points are tilted at an angle somewhat steeper than 1, so there is some departure from compensation. The magnitudes of $\alpha\Delta\theta$ and $\beta\Delta S$ reported on the axes depend on the quality factor Q. For smaller Q the wavelet is less selective in wavenumber space, and the wavelet coefficients are larger because they account for variability over a wider range of wavenumbers. However, the shapes of the PDFs are independent of these details, and using a different Q does not change any of the results of this paper.

Joint PDFs of the thermohaline fluctuations emphasize the distinction between typical fronts, in the center of the PDFs, and extreme fronts, in the tails. Typical temperature and salinity fronts cluster near the origin and are not as well compensated as large ones; that is, the red clouds in the center of the contour plots are not as elongated as the blue tails. The distinction between the two populations is especially evident at scales smaller than 100 m. A blowup of the central region of the joint PDF for a wavelength of 20 m demonstrates that the ratio of the major to the minor axis of the cloud of points approaches 1 for the weakest fluctuations (Plate 4): at short wavelengths compensation is not ubiquitous but is a feature of the strongest fronts.

A consideration of two different measures of the density ratio is used to show how R varies with scale and frontal strength. One measure of the density ratio for a given wavelength is the slope of the principal axis of the joint PDFs shown in Plate 3. The principal axis is found by setting the covariance between temperature and salinity wavelet coefficients to zero. Being a quadratic measure, it is especially sensitive to the largest fronts. The slope of the principal axis is a bit larger than unity, between 1.1 and 1.4, for all scales between 20 m and 10 km (Figure 2). A second measure of the typical density ratio is the median ratio of the wavelet coefficients of temperature and salinity. The median is a robust estimator in the sense that it is not particularly sensitive to outliers. The median density ratio is less than the slope of the principal axis at all wavelengths (Figure 2) because small changes of temperature and salinity are less correlated than are large ones. The median is close to 1 at large scales and drops abruptly at wavelengths smaller than 100 m.

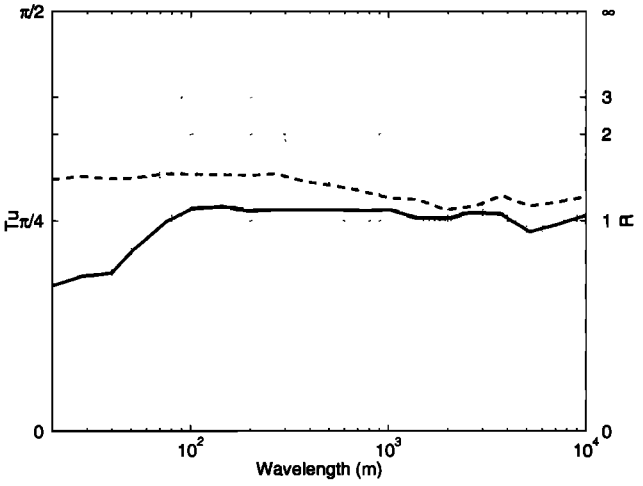

Figure 2. Density ratio as a function of wavelength computed as a median ratio (solid line) and as the slope of the principal axis (dashed line) of the wavelet coefficients for T and S at 50 dbar. The right axis shows values of density ratio R, while the left axis shows the corresponding values of Turner angle Tu. The principal axis estimate of the density ratio is strongly influenced by the strongest fronts and remains between 1.1 and 1.4. The median of the density ratio is near 1 at wavelengths down to 100 m. Below 100 m the median drops suddenly and is 0.6 at a scale of 20 m.

The PDFs of the Turner angle help to interpret the differences between the median density ratio and the slope of the principal axis (Figure 3). These PDFs have a single mode at R between 1 and 1.6 at all scales between 20 m and 10 km. The slope of the principal axis and the mode differ at most by 0.3 (if the statistics of the wavelet coefficients $\alpha\Delta\theta$ and $\beta\Delta S$ were Gaussian, the two parameters would coincide). The median density ratio is close to the slope of the principal axis at scales larger than 100 m because, at these scales, fronts are typically compensated. At scales smaller than 100 m a large fraction of temperature and salinity fluctuations are poorly correlated and are as likely to assume any value of density ratio. Therefore the PDFs are composed of a uniform distribution, due to uncorrelated weak T-S fluctuations and a peak due to few compen-

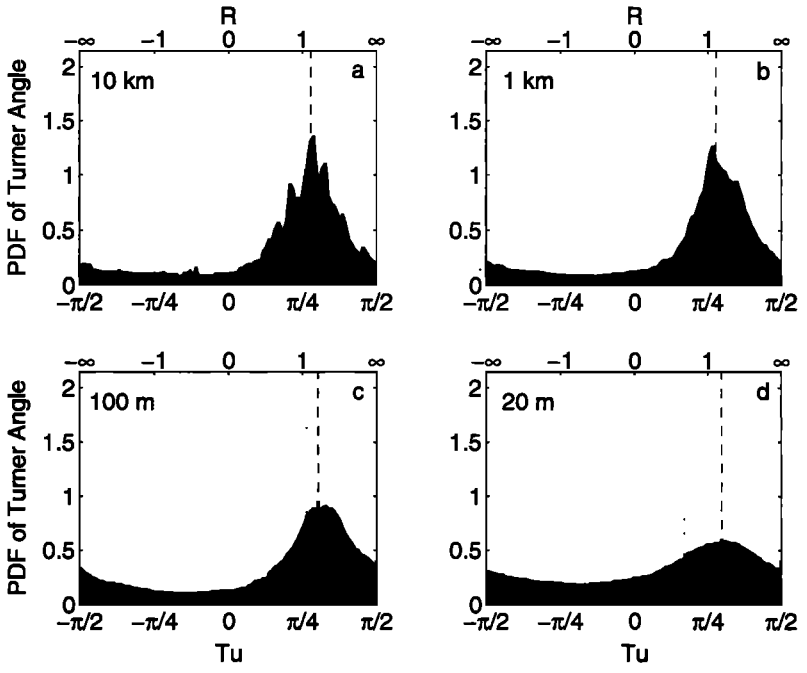

Figure 3. Probability density functions of the Turner angle for measurements along 50 dbar at wavelengths of (a) 10 km, (b) 1 km, (c) 100 m and (d) 20 m. The dashed and the dotted lines are the slope of the principal axis and the median R of the wavelet coefficients of temperature and salinity at that wavelength. The distributions have a single mode between 1 and 1.6 (within 0.3 of the slope of the principal axis). The number of points in the tails increases suddenly at scales smaller than 100 m, indicating the presence of numerous uncorrelated thermohaline fluctuations.

sated strong fronts. The flattening of the PDFs is reflected in the sudden drop of the median density ratio.

Uncertainties in the estimated horizontal density ratio have a number of different causes. Standard errors, calculated with a bootstrap method [*Efron,* 1982], are < 0.004 for the median density ratio and < 0.01 for the slope of the principal axis. Statistical uncertainties in these estimates are relatively small because of the large amount of data. Errors due to contamination of the data from profiling vertical stratification and from instrumental noise are more difficult to quantify. The effect of variability introduced by the vertical displacements of the SeaSoar is addressed by repeating the calculations of the density ratio on a subset of data obtained at crossings of the 50 dbar surface. Crossings are computed by linearly interpolating T and S between measurements 1 s apart that cross the pressure surface. The density ratio is estimated at each wavelength by using all differences of temperature and salinity available for separations within 10% of that wavelength. The median R and the slope of the principal axis remain within 0.06 of the values shown in Figure 2, at all wavelengths. Therefore the vertical displacements of the SeaSoar have a small effect on estimates of R. Variability due to instrumental error is modeled as the difference between the T and S measurements of the two sets of sensors mounted on the SeaSoar (divided by $\sqrt{2}$ under the assumption that instrumental noises in the two sensors are independent). This estimate of the noise is likely an overestimate because it includes instrumental errors as well as real thermohaline variability at scales smaller than the distance between the two sets of sensors (72 cm). The sensitivity of estimates of the density ratio to this noise is addressed by performing the wavelet analysis on data with a constant density ratio at all scales, corrupted with the signals obtained from the differences of the two sets of sensors. Monte Carlo simulations show that the effect of this noise is null on the slope of the principal axis and 0.1 on the median R, even at the smallest scales. Therefore both profiling of vertical stratification and instrumental noise can be excluded as explanations for the sudden drop of the median R at wavelengths shorter than 100 m.

The ubiquitous presence of compensated thermohaline gradients supports recent theoretical ideas on the horizontal dynamics of the mixed layer. *Young* [1994] and *Ferrari and Young* [1997] suggest that mixing driven by density gradients is more effective than mixing that homogenizes both the thermal and haline components indiscriminately; that is, the mixed layer mixes horizontally in such a way that density gradients are dissipated, while compensated temperature and salinity gradients persist. A horizontal diffusivity equal for temperature and salinity but dependent on horizontal density gradient reproduces this behavior.

Measurements show that temperature and salinity

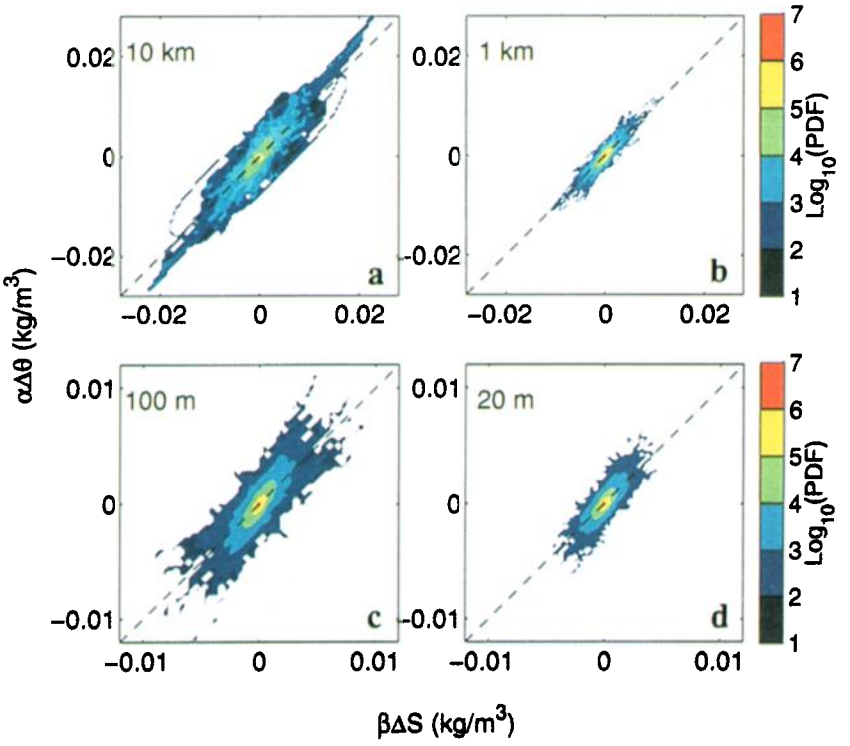

Plate 3. Joint probability density functions of the wavelet coefficients of potential temperature $\alpha\Delta\theta$ and salinity $\beta\Delta S$ at wavelengths of (a) 10 km, (b) 1 km, (c) 100 m and (d) 20 m for measurements along 50 dbar. The dashed black lines have a slope of 1. The points in the tails of the distributions are elongated along the slope of 1, indicating a tendency for large gradients to cancel each other in their effect on density. The shape of the distributions, extremely peaked in the center and with long tails, suggests that the horizontal structure of the mixed layer is formed by relatively few strong density-compensated fronts separated by regions of weak thermohaline variability.

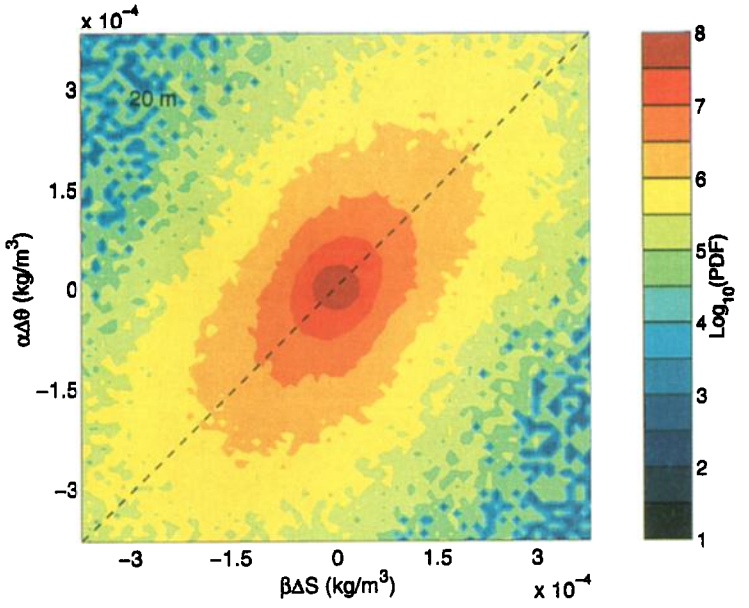

Plate 4. An enlargement of the center of Plate 3d. Note the change in the colors of the contour intervals. The central peak is nearly circular and not elongated along the slope of 1. At this scale, typical fluctuations of temperature and salinity are poorly correlated.

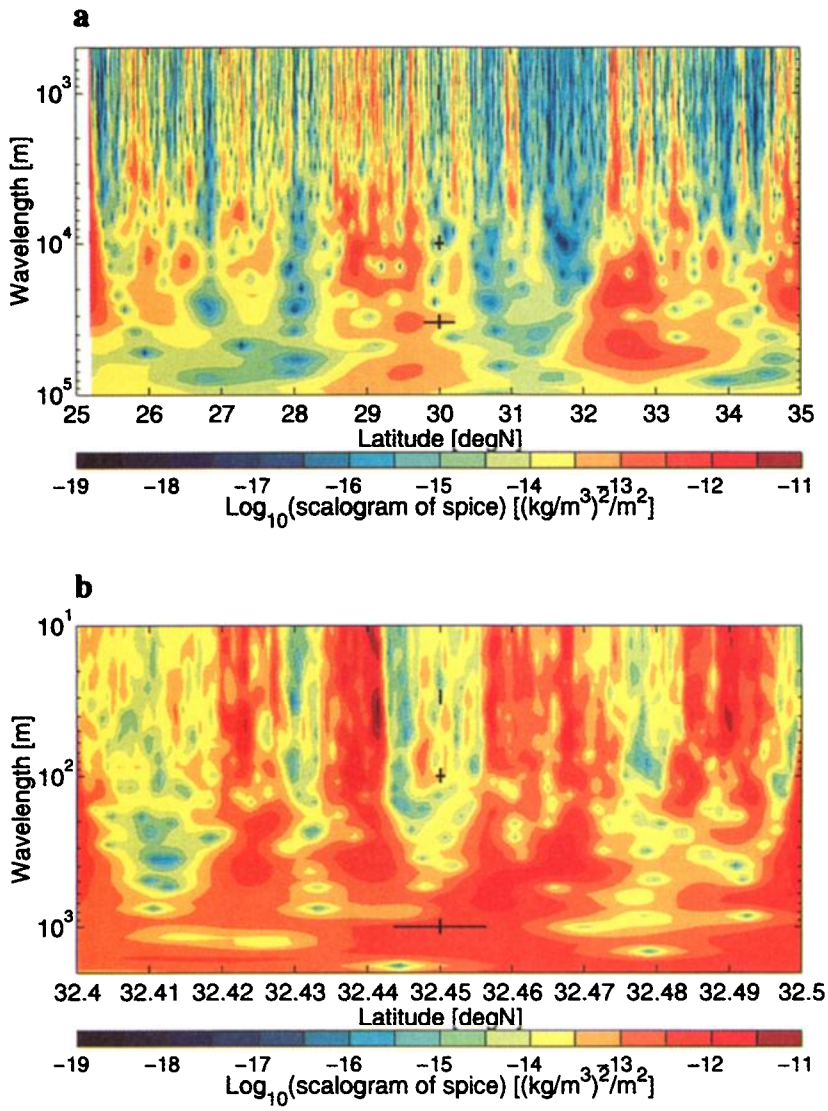

Plate 5. Wavelet scalograms of spice along 50 dbar in the mixed layer. (a) Spice scalogram for wavelengths between 100 km and 500 m. (b) Spice scalogram of a section 11 km long, also shown in Plate 2c, for wavelengths between 2 km and 10 m. The black crosses are twice the square roots of the second moments of the wavelet functions squared in location and wavelength domains and indicate the resolution of the analyzing wavelet. Resolution in space and in wavelength increase toward the top (note that the vertical axis is logarithmic). High values in the scalogram indicate regions of strong spice gradients. High and low values show up in vertical stripes and imply that small-scale gradients tend to be particularly large at large-scale fronts.

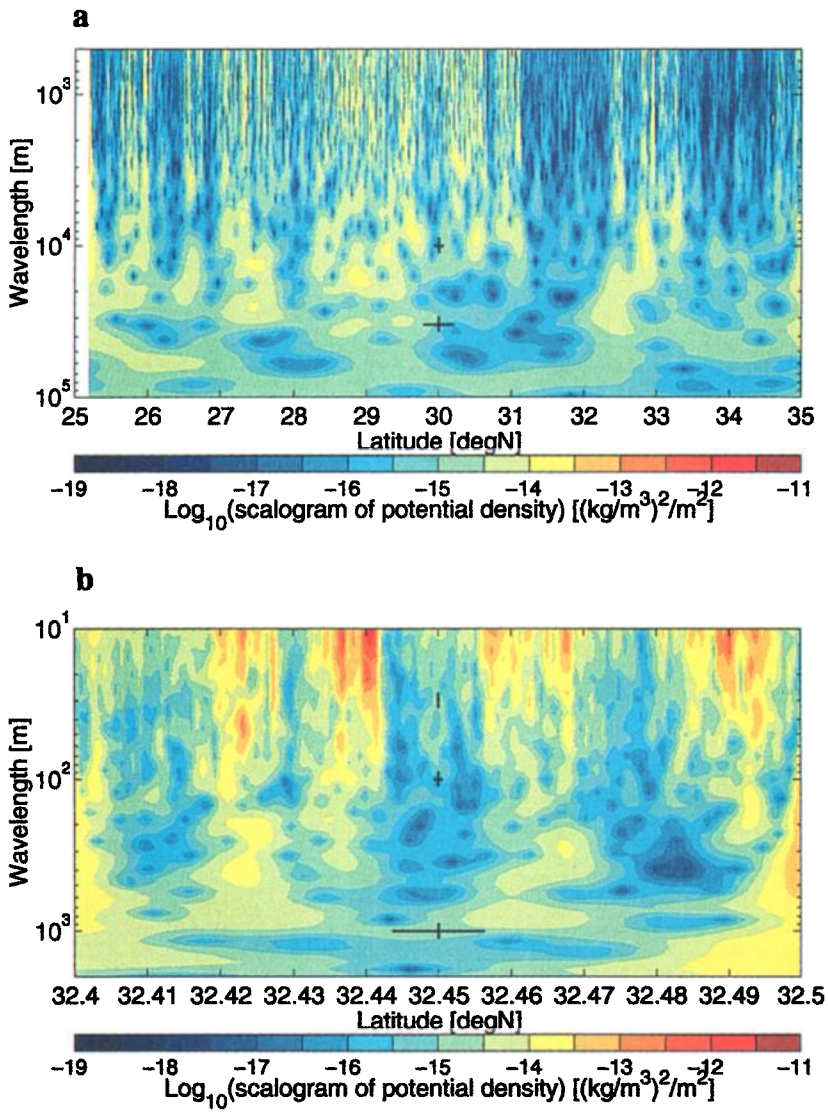

Plate 6. Wavelet scalograms of potential density along 50 dbar in the mixed layer for the same sections shown in Plate 5. The spectral levels of potential density are a couple of orders of magnitude smaller than those of spice, indicating that most of the temperature and salinity variance is compensated. Variability peaks in the same location at all wavelengths as for spice. Bands of high variability appear at wavelengths shorter than 100 m, showing that compensation is not as typical at those scales.

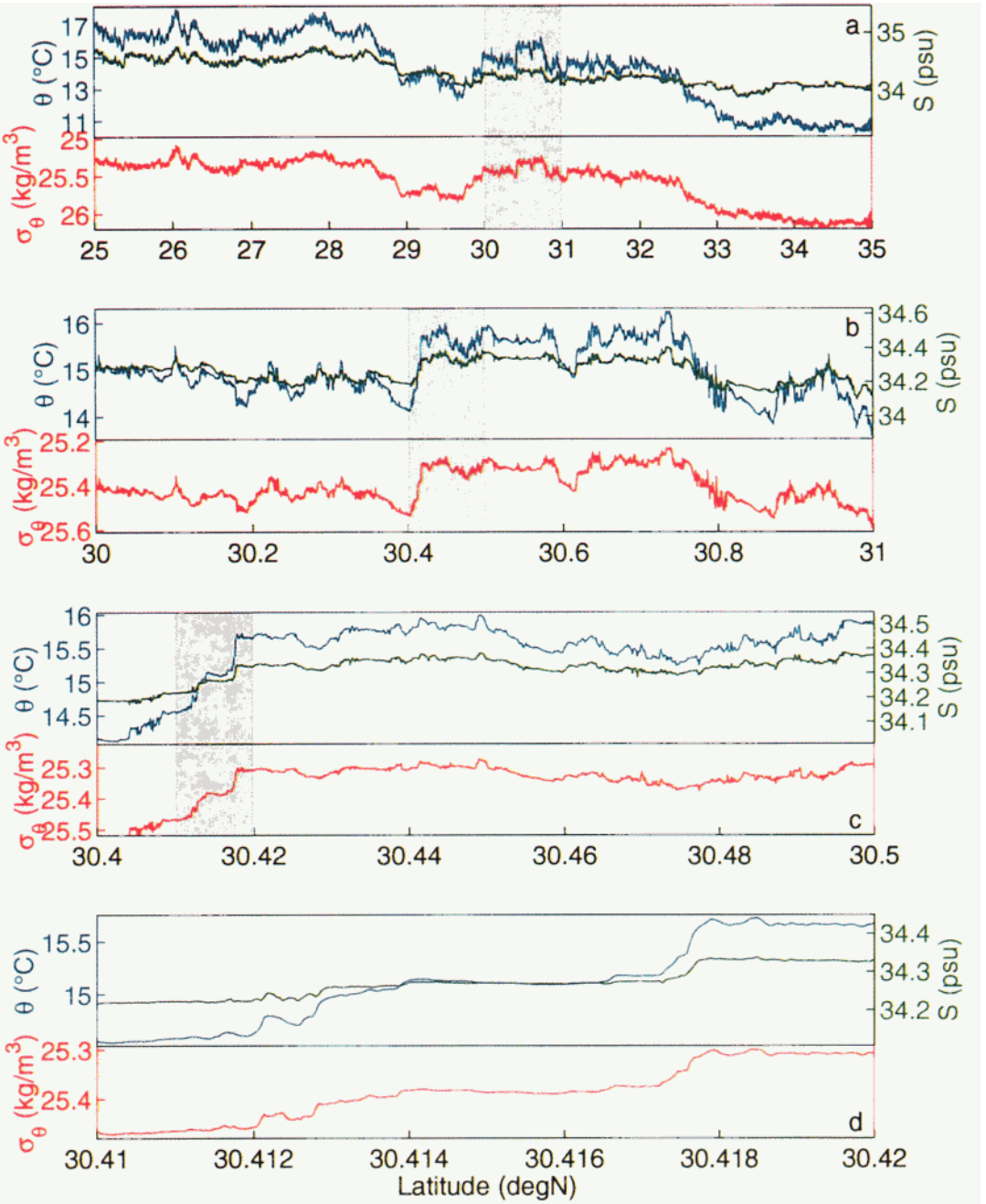

Plate 7. Potential temperature θ (blue lines), salinity S (green lines), and potential density σ_θ (red lines) as in Plate 2 but along the 200 dbar pressure surface. Salinity fluctuations are proportional and opposite to those of temperature at all scales but do not cancel completely the effect of temperature on density because horizontal tows in the thermocline include diapycnal signal due to the tilt of isopycnal surfaces.

fronts tend to be compensated at all scales between 100 m and 10 km. At scales below 100 m, compensation depends on frontal strength, as shown by the difference in the median R and the slope of the principal axis; that is, strong fronts tend to be more compensated than weak fronts. The decrease in the median density ratio reflects a change in the thermohaline dynamics of the mixed layer. The dominant turbulent eddies that stir the mixed layer have an aspect ratio close to 1 and a size close to 100 m (the depth of the mixed layer in the region of the survey). These turbulent eddies may be Langmuir cells, driven by wind and surface waves, or convection cells, driven by negative buoyancy fluxes at the surface. The process of slumping and mixing is valid only at scales larger than the turbulent eddy scale [*Ferrari and Young*, 1997]. At smaller scales the relationship between temperature and salinity can break down in the absence of strong density gradients because mechanical stirring homogenizes temperature and salinity anomalies indiscriminately and does not select any particular density ratio. On the other hand the strongest density fronts slump under the action of gravity at all scales, and T-S compensation is seen for the largest gradients down to 20 m.

3.2. Wavelength and Location Dependence of Mixed Layer Thermohaline Variability

Measurements along 50 dbar are analyzed to investigate the distribution of thermohaline variability as a function of wavelength and location. Surface fluxes and entrainment create horizontal thermohaline anomalies in the mixed layer. In section 3.1, the analysis showed that the internal dynamics destroys temperature and salinity gradients that happen to produce density gradients. The goal in this section is to study the effect of stirring of thermohaline anomalies by horizontal flows, either geostrophic or wind driven. The hypothesis is that stirring cascades thermohaline variability down to small scales, in a way similar to that described by *Batchelor* [1959] for a passive tracer advected by a homogeneous and isotropic velocity field.

Horizontal profiles of temperature and salinity along 50 dbar are extremely intermittent. A systematic examination of succeeding enlargements of the profiles in Plate 2a reinforces the impression that T and S are typically uniform, except in confined regions where they change abruptly. These abrupt changes form frontal regions characterized by fluctuations on all scales from several kilometers down to 10 meters. Suitable analysis tools are now discussed for determining and interpreting the correlations of thermohaline variability between different scales.

Temperature and salinity are strongly coherent in the mixed layer. Therefore an analysis of thermohaline variability in terms of T and S would be quite redundant. Working with potential density and a state variable defined to be sensitive only to fluctuations of temperature and salinity along isopycnals is more convenient. Such a variable is usually defined to increase for hot and salty water and has come to be named *spice* (*Veronis* [1972] introduced this variable, and *Munk* [1981] used the word spiciness). For small fluctuations of temperature and salinity, spice variations $\Delta\tau$ are defined as the thermohaline variations locally orthogonal to density in a T-S plane rescaled with the local expansion coefficients,

$$\Delta\tau = \alpha\Delta\theta + \beta\Delta S$$

The differences $\Delta\theta$ and ΔS are calculated over some spatial interval, and the expansion coefficients, α and β, are averaged over the same interval. A global definition of spice is necessary when analyzing large thermohaline fluctuations [*Veronis*, 1972; *Jackett and McDougall*, 1985]. For the purpose of this paper a local definition is preferable because spice is used to characterize thermohaline variability over a T-S range for which the equation of state for seawater is approximately linear.

The distribution of spice and potential density variability in location and wavelength is given by the squared magnitudes of the wavelet coefficients, hereinafter referred to as a wavelet scalogram. Wavelet coefficients are computed as discussed in section 3.1 (wavelet coefficients of spice are the sum of wavelet coefficients of temperature and salinity in density units). The normalization of the coefficients used in this section ensures that the integral of the wavelet scalograms across all wavelengths and all latitudes gives the total spice and potential density variance. The wavelet scalograms are in units of density squared per unit wavelength, per unit distance; that is, $(\mathrm{kg\ m^{-3}})^2\ \mathrm{m^{-2}}$ (see Appendix B). Scalograms are the result of an integral transform and are analogous to periodograms computed with a Fourier transform. Spectra are statistical measures of the distribution of energy density as a function of wavelength and are obtained by averaging wavelet scalograms over all locations and Fourier periodograms over wavelength bands. The degrees of freedom of these estimates depend on the number of wavelengths over which the average is carried. In wavelet analysis this value is set by the quality factor Q. Wavelets are therefore appropriate for this study because by maintaining Q constant they trade off resolution in wavelength for resolution in location as needed to resolve the details of the thermohaline signals at different wavelengths.

The scalogram of spice along 50 dbar for wavelengths between 100 km and 500 m is plotted in Plate 5a. The first 20 km of the tow are not included in Plate 5a because tuning the control system of the SeaSoar to follow accurately the isobar took slightly over an hour. The two confined regions with high spice energy density at scales larger than 10 km correspond to the two largest frontal regions visible in Plate 2a, one between 29° and 30°N and the other between 32° and 33°N. The scalograms are characterized by vertical stripes of high variability at all scales separated by regions where variability is 6 to 7 orders of magnitude smaller. Only

in the presence of a large-scale gradient do appreciable thermohaline fluctuations at small scales exist. If the wavelet scalogram is averaged over regions of high variability, spectra are white as a function of wavelength. The same is true for regions with low variability, but the spectral levels are much smaller. Spectra flat as a function of wavelength l are red as a function of wavenumber k because variability per unit wavelength is equivalent to variability per unit wavenumber times k^{-2}. The spectral slope holds all the way down to scales of 10 m. A blow-up of the spice scalogram shown in the lower panel of Plate 5b visually demonstrates that high variability becomes more intermittent at small scales and is localized in the same regions from wavelengths of kilometers down to meters.

The wavelet scalogram of potential density at wavelengths longer than 100 m shows patterns similar to that of spice, but the energy levels are a couple of orders of magnitude smaller (Plate 6). Such a difference between spice and potential density variability indicates that large thermohaline fluctuations are typically compensated in the mixed layer. Potential density variability of a smaller section of data illustrates that compensation begins to fail at scales shorter than 100 m and density fluctuations become comparable to compensated T-S fluctuations (Plates 5b and 6b). Breaking of compensation at scales shorter than 100 is consistent with the results obtained in the analysis of the density ratio.

Colocated variability at different scales is observed both in spice and in potential density scalograms; the mechanism responsible for this colocation does not distinguish between active (density) and passive (spice) scalars. The signature of large-scale fronts at small scales is likely to be generated by geostrophic and wind-driven velocity fields that horizontally stir the mixed layer. Stirring produces small scale fluctuations only at large-scale T and S fronts, where there is thermohaline structure to be stirred. In regions with strong temperature and salinity anomalies the velocity field transfers the high variability down to the scales of dissipation. In regions with little thermohaline structure the process is analogous, but the variability transferred is orders of magnitude smaller.

The structure of the temperature and salinity fields, composed of frontal zones with large gradients separated by regions of small gradients, is characteristic of passive scalars advected by a stirring field. The PDFs of the wavelet coefficients for T and S depart strongly from Gaussians and develop exponential tails at small scales. The kurtosis goes from a nearly Gaussian value of 4 at 10 km to values in excess of 80 at 20 m. Qualitatively similar distributions are predicted for fluctuations of passive scalars advected by a random velocity field [*Sinai and Yakhot,* 1989; *Danaila et al.,* 1999].

4. Thermohaline Gradients in the Upper Thermocline

Measurements along a shallow isobar in the mixed layer have been used to show that lateral changes in temperature and salinity are largely compensated on scales from 20 m to 10 km. This result cannot hold in the waters of the thermocline where density differences due to temperature exceed density differences due to salinity to produce the observed density stratification. Data along the 200 dbar isobar and along the 24.8 kg m^{-3} and 25.5 kg m^{-3} isopycnals are now used to investigate the T-S relationship of the upper thermocline and to describe the changes in thermohaline variability across the base of the mixed layer.

4.1. Thermohaline Variability Along an Isobar in the Upper Thermocline

An accurate measurement of both temperature and salinity on varying horizontal scales in the thermocline has been the goal of several studies in the past. For instance, *Mack* [1989] and *Dugan et al.* [1992] report on towed chain measurements of temperature and conductivity, *Magnell* [1976] and *Garrett and Schmitt* [1982] show data from horizontal tows. These studies focus on variability on scales of cm to 100 m. Notably, *Samelson and Paulson* [1988] studied larger scales using a 1400 km tow of a thermistor chain, but the only salinity data are from the surface and are, of necessity, heavily smoothed because they derive from ship's intake. During the Spice experiment both temperature and salinity were measured in the thermocline on horizontal scales from 4 m to ~1100 km.

Profiles of potential temperature, salinity, and potential density are shown in Plate 7 for a tow along 200 dbar, an isobar chosen to remain well beneath the base of the mixed layer at all latitudes. Every density fluctuation due to temperature is opposed by a smaller one due to salinity at all observed scales down to 10 m, the smallest scales visible in Plate 7d. The control system maintained the vehicle within an RMS of 0.4 dbar from the pressure surface of 200 dbar and contamination of horizontal temperature and salinity measurements by the vertical excursions of the SeaSoar is minor (Figure 4). Plate 7d and Figure 4d offer visual evidence that the measured T-S profiles describe real horizontal variability. During the time shown in that section the control system performed worse than usual, and the vertical displacements are quite large; yet the fronts in temperature and salinity are not correlated with pressure. Only in regions of weak horizontal thermohaline variability, vertical fluctuations contaminate the T-S horizontal profiles. Measurements of pressure are used to eliminate this undesired signal. First, ver-

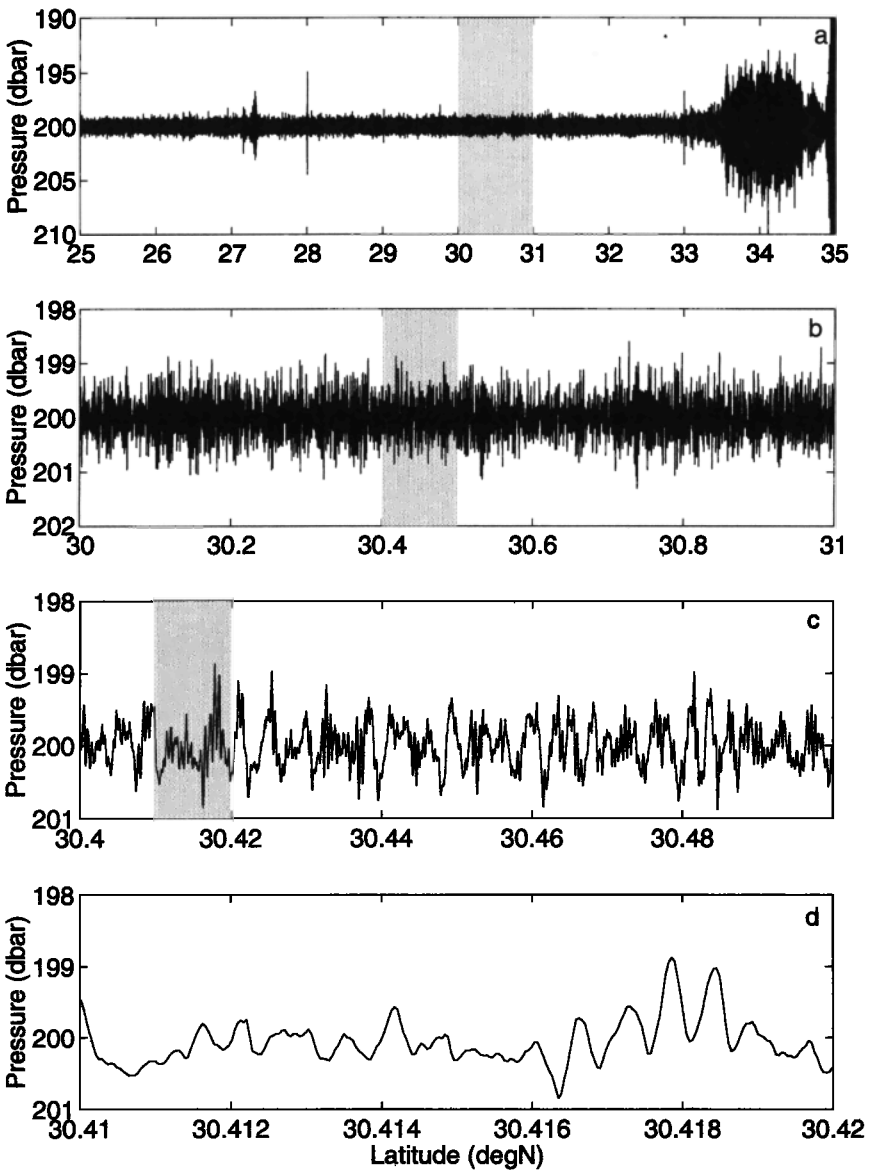

Figure 4. Pressure fluctuations measured by the SeaSoar during the isobar tow at 200 dbar. Pressure is not correlated with the thermohaline fields, proving that the strong fronts in Plate 7 are not due to profiling vertical stratification but reflect true horizontal variability. In this section the SeaSoar was towed from north to south, and the large excursions between 33.3° and 35°N occurred while tuning the control system. After this first transient the RMS pressure fluctuations were 0.4 dbar.

tical T and S gradients are computed as that part of T and S that is correlated with pressure on sections of 250 s ($\sim$1 km in length). Then, the signal produced by pressure excursions through the estimated vertical gradients is subtracted from the measurements of T and S. This correction removes the effect of vertical stratification averaged over a horizontal scale of 1 km. Contamination due to changes in stratification over horizontal scales of < 1 km and vertical scales of < 0.4 m is not eliminated.

Wavelet coefficients of temperature and salinity are calculated for wavelengths between 20 m and 10 km, and their joint PDFs are displayed in Plate 8. Data north of 33.3°N are not used in the analysis because at the beginning of this southward going tow the controller was not tuned yet and vertical oscillations of the SeaSoar were quite large (Figure 4). The joint PDFs are in the form of clouds elongated along a slope slightly steeper than 2, indicating a tendency for density variations due to temperature to exceed density variations due to salinity by a factor of ~ 2. The correlation between the wavelet coefficients of T and S is extremely tight at scales > 1 km. At smaller scales an increasing number of coefficients cluster in a circular cloud near the origin. The PDFs become the superposition of two different populations: the large thermohaline gradients

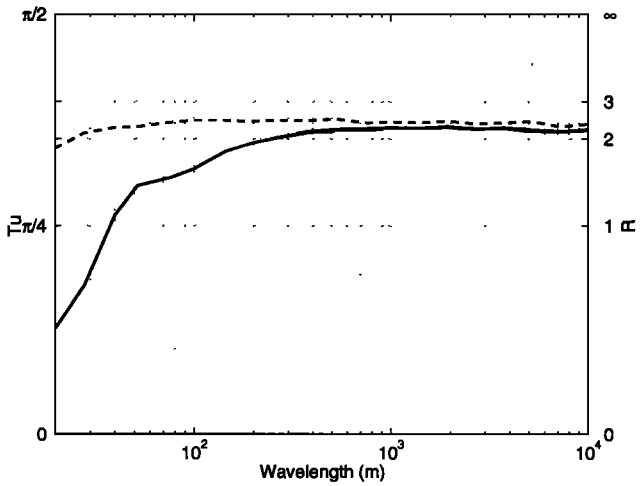

Figure 5. Density ratio at 200 dbar as a function of wavelength computed as a median ratio (solid line) and as the slope of the principal axis (dashed line). The principal axis estimate of the density ratio is greatly influenced by the strongest fronts and remains nearly constant at 2.4 for scales between 10 km and 80 m. At smaller scales it decreases slightly. The median of the density ratio is near 2.2 at wavelengths larger than 500 m. At shorter wavelengths it drops and is 0.4 at 20 m.

in the tails, characterized by a tight correlation, and the weak gradients in the center, for which the the correlation is quite poor.

The median density ratio and the slope of the principal axis of the thermohaline gradients are used to study how compensation varies with scale and frontal strength. The slope of the principal axis of the joint PDFs is nearly constant at 2.4 for scales between 10 km and 40 m but decreases slightly at smaller scales to become 1.8 at 20 m (Figure 5). The median R is less than the slope of the principal axis at all wavelengths (Figure 5), because small fluctuations of T and S are less correlated than large ones. The median is close to 2.2 at large scales, starts decreasing at wavelengths smaller than ~ 300 m, and drops abruptly below 50 m. The PDFs of the Turner angle have a single mode within 0.1 of the principal axis at all wavelengths, proving that typical salinity gradients oppose temperature stratification (Figure 6). At scales of 100 and 20 m, a large fraction of uncorrelated weak temperature and salinity gradients fills the tails of the PDFs and consequently the peaks decrease. This change in shape of the PDFs is captured by the drop in the median R at small scales.

Uncertainties in the estimates of the density ratio are now investigated. Standard errors, calculated with a bootstrap method, are < 0.005 for the median density ratio and < 0.05 for the slope of the principal axis. Errors due to contamination of the data from the vertical motion of the SeaSoar are not significant, as is proved by calculating the density ratio on a subset of data obtained by interpolating T and S on crossings of the 200 dbar surface. Both the median R and the slope of the principal axis remain at all scales within 0.1 of the values shown in Figure 5. Instrumental error, estimated with the same Monte Carlo technique used for the analysis of the 50 dbar tow, explains 50% of

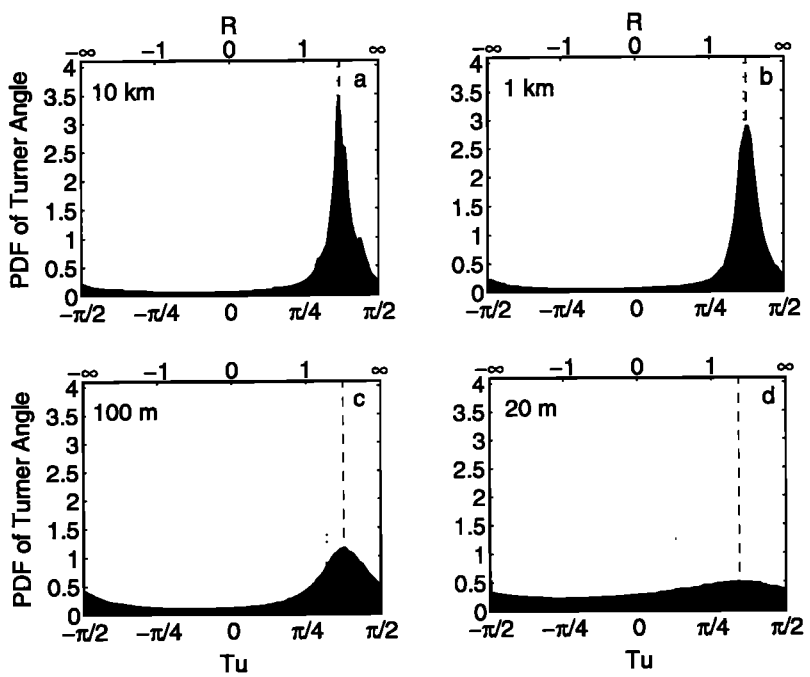

Figure 6. Probability density function of the Turner angle at wavelengths of (a) 10 km, (b) 1 km, (c) 100 m, and (d) 20 m along the 200 dbar isobar. The dashed and the dotted lines are the slope of the principal axis and the median R of the wavelet coefficients of temperature and salinity at that wavelength. The distributions have a single mode between 2.4 and 1.8 (within 0.1 of the slope of the principal axis). The peak of the PDF broadens at scales shorter than 500 m, indicating the presence of numerous uncorrelated thermohaline fluctuations.

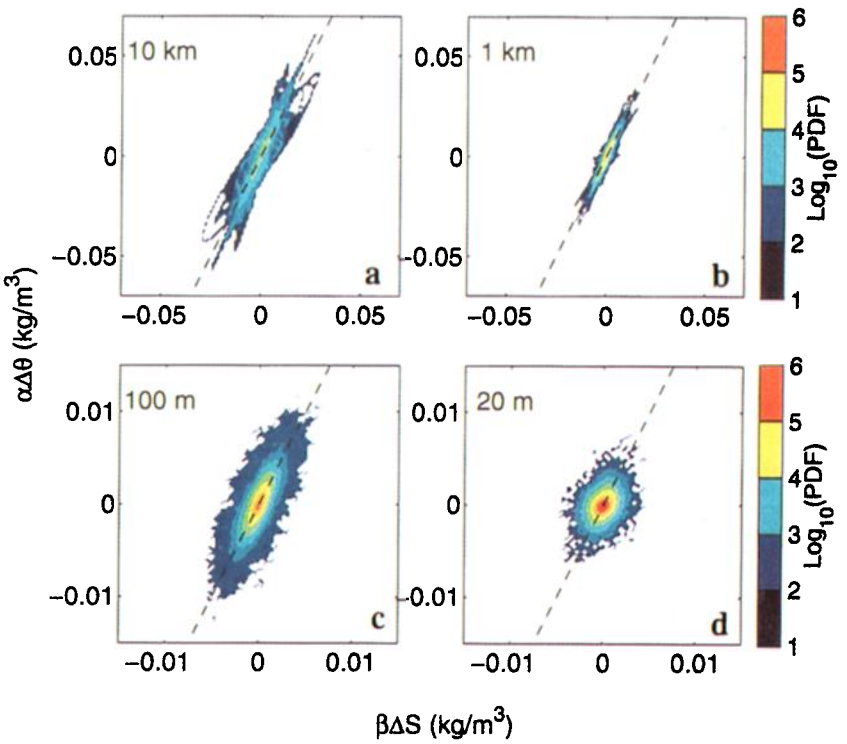

Plate 8. Joint PDFs of the wavelet coefficients of temperature $\alpha\Delta\theta$ and salinity $\beta\Delta S$ at wavelengths of (a) 10 km, (b) 1 km, (c) 100 m and (d) 20 m for measurements along 200 dbar. The dashed black lines have a slope of 2. Points in the tails of the distributions extend along a slope slightly steeper than 2, indicating a tendency for the density changes due to salinity to oppose partly those due to temperature. At small scales the correlation is not as tight as at large scales.

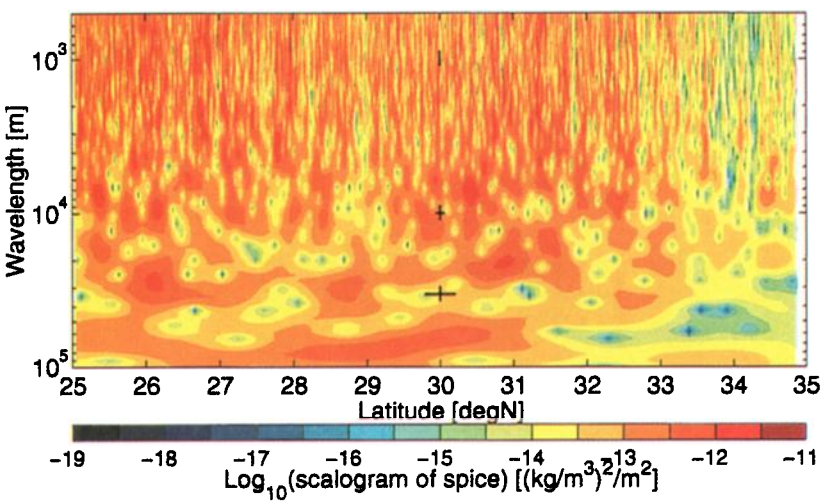

Plate 9. Wavelet scalogram of spice along the 200 dbar isobar in the thermocline. Spice variability along isobars in the thermocline is uniformly distributed at all wavelengths and locations.

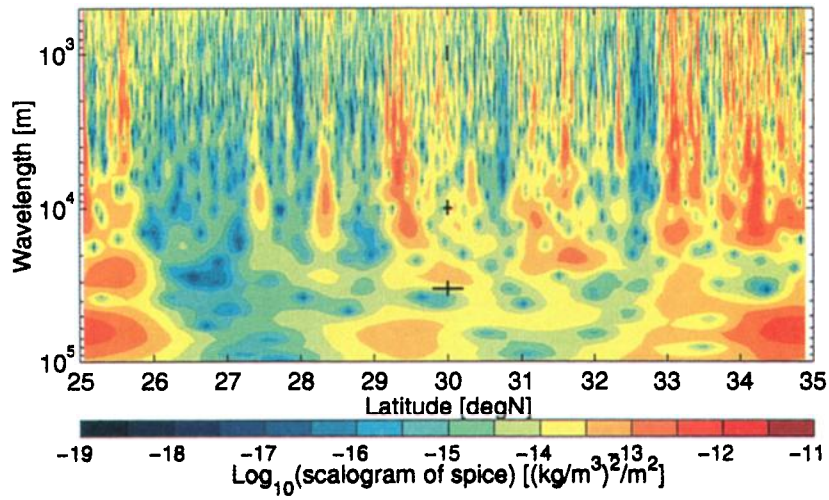

Plate 10. Wavelet scalogram of spice along the 25.5 kg m^{-3} isopycnal. Spice variability is typically an order of magnitude smaller along this isopycnal than along 200 dbar. High bursts of variability appear at all length scales in the same locations.

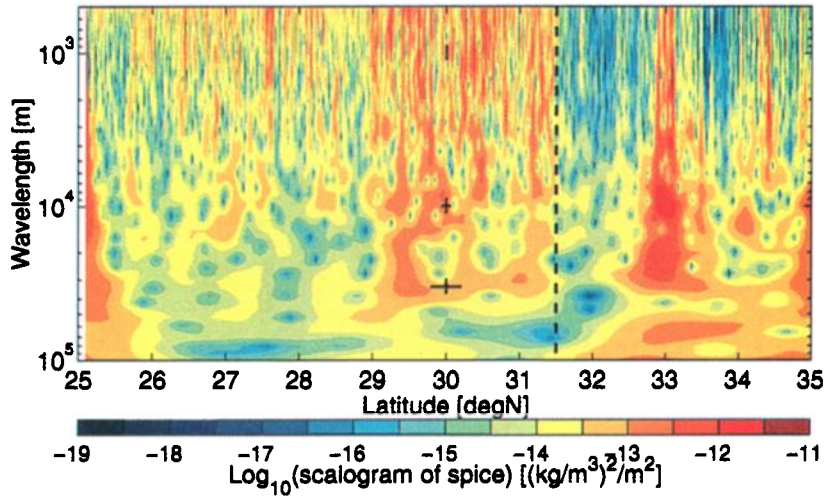

Plate 11. Wavelet scalogram of spice along the 24.8 kg m^{-3} isopycnal between 25° and 31.5°N. North of 31.5°N, i.e. to the right of the dashed vertical line, no more water of density 24.8 kg m^{-3} is found and the scalogram of spice is measured along the 50 dbar isobar. The isopycnal 24.8 kg m^{-3} sits at the base of the mixed layer for latitudes between 25° and 28.8°N and then crosses into the mixed layer. At 31.5°N the isopycnal outcrops. Spice variability along the isopycnal is lower in the thermocline than in the mixed layer. Stripiness in the scalogram is more evident for measurements in the mixed layer, both along the isopycnal and the isobar.

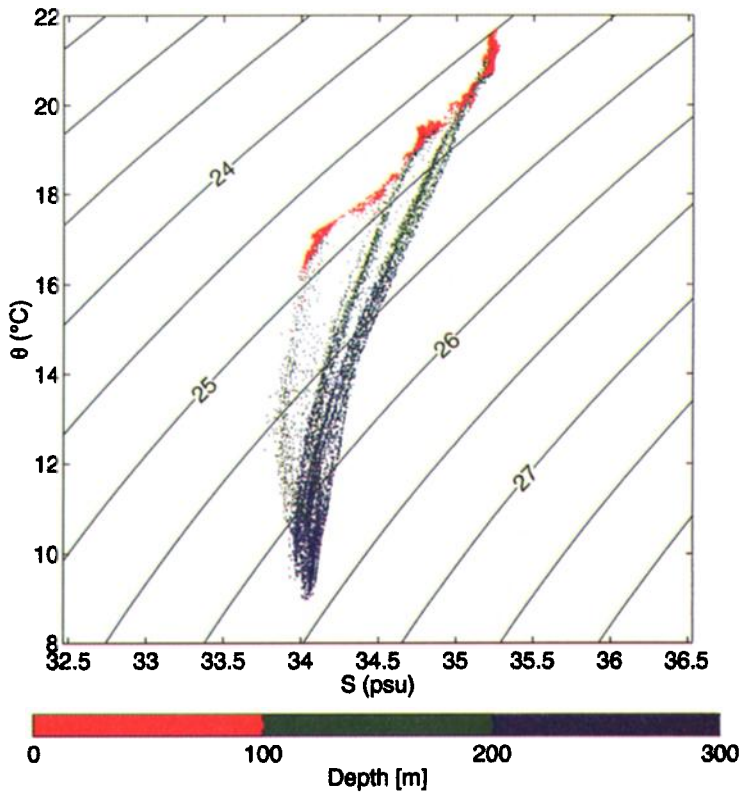

Plate 12. Potential temperature versus salinity for measurements collected between the surface and 300 m by profiling along a sawtooth pattern. The axes for potential temperature and salinity are scaled by the thermal and haline expansion coefficients calculated for the average temperature and salinity. Thermohaline variability is mostly along isopycnals in the mixed layer (red points) and develops a diapycnal component at depth (green and blue points).

the drop at scales shorter than 50 m in the principal axis and the median R. This noise affects estimates of density ratio in the thermocline more than in the mixed layer because the variance of the difference between measurements from the two sets of sensors is 3 times larger at 200 dbar than at 50 dbar. This increase in variance can be due to the degraded performance of the control system and the sensors at depth as well as to real variability on scales shorter than the separation of the sensors. Separating the relative contribution of these sources of variability is not possible and part of the loss in T-S correlation at small scales could be an artifact of the measurement procedure.

The horizontal density ratio in the thermocline is not 1 because internal waves and geostrophic eddies displace isopycnal surfaces in the vertical and create horizontal density gradients. Every time the SeaSoar crosses a tilted isopycnal, the sensors measure a density difference due to temperature that is twice and opposite to that due to salinity. This is consistent with previous observations [*Schmitt and Evans*, 1978] that most T-S relationships of the upper thermocline in the subtropical oceans are described by a density ratio between 2 and 3. Schmitt and Evans studied vertical T-S profiles from hydrographic stations, while the present analysis uses horizontal profiles. The density ratio is the same over vertical and horizontal sections because thermohaline gradients are much larger across than along isopycnals in the strongly stratified waters of the thermocline. Therefore, as long as the profiles intersect isopycnal surfaces, the density ratio measured is diapycnal. At horizontal scales shorter than $\sim$300 m, the SeaSoar does not cross isopycnals as often as at large scales. The diapycnal density ratio is still close to 2, as shown by the principal axis, but the median R drops because the horizontal profiles are characterized by numerous regions of weak and uncorrelated temperature and salinity gradients. Mixing generated by breaking internal waves and shear instabilities is a likely cause of patches of uniform temperature and salinity with horizontal scales of hundreds of meters and vertical scales of a few meters [*Mack*, 1989].

4.2. Thermohaline Variability Along and Across Isopycnals in the Upper Thermocline

Distributions of heat and salt in the ocean thermocline depend on mixing and stirring along and across density surfaces. In the past the focus has been on

measurements of the vertical structure of the thermocline, which is dominated by diapycnal gradients. During the Spice experiment, T-S measurements were collected along isobars and isopycnals and provided an ideal data set to contrast the thermohaline structure along and across isopycnals.

The wavelet scalogram of spice along 200 dbar shows the distribution of thermohaline variability along an isobar in the thermocline for wavelengths between 500 m and 100 km in the latitude range between 25° and 35°N (Plate 9). The 200 dbar scalogram looks very different from that along 50 dbar in the mixed layer (Plate 5). Spice variability along 200 dbar is spread uniformly through all wavelengths and locations, while in the mixed layer bands of high variability are separated by relatively calm regions. In the thermocline the internal wave field displaces surfaces of constant density at all latitudes and wavelengths. Thus horizontal profiles of temperature and salinity are dominated by the diapycnal gradients created by the tilting of isopycnals. The spectrum of potential density is at all wavelengths within a factor of 2 of the empirical Garrett–Munk prediction for internal waves [*Garrett and Munk*, 1975]. Potential density and spice spectra are both red with a slope of -2, but spectral levels for spice are 8 to 10 times larger. This disparity in energy levels is a result of the competing effects of temperature and salinity on density; if temperature and salinity were perfectly correlated with a density ratio of 2, the spice variance would be 9 times the density variance.

Towing the SeaSoar along isopycnal surfaces filters out the internal wave variability. The wavelet scalogram of spice along the isopycnal 25.5 kg m^{-3}, shown in Plate 10, is different from that along 200 dbar, even though the two surfaces span the same waters for most of the tows. Along 25.5 kg m^{-3} energy densities are at least an order of magnitude smaller, and variability is intermittent: stripes of high energy at all wavelengths are separated by relatively uniform regions. This structure is similar to that seen at 50 dbar in the mixed layer. In both cases the colocation of thermohaline variability at different wavelengths is created by stirring fields that are horizontal in the mixed layer and along isopycnals in the thermocline, where the dynamics are mostly geostrophic. Horizontal tows in the thermocline do not show these colocations because the diapycnal gradients due to the tilting of isopycnals are larger than those generated by stirring along isopycnals.

A tow along the 24.8 kg m^{-3} isopycnal helps to address the question of how the thermohaline structure observed in the mixed layer is modified as waters are subducted in the thermocline. This isopycnal sits right at the base of the mixed layer from 25° to 28.8°N, where it crosses into the mixed layer (shallow jagged white line in Plate 1). The scalogram of spice along this tow is composed of three different regions (Plate 11). Between 25° and 28.8°N the isopycnal meanders at the base of the mixed layer. The spectral levels are similar to those measured along 25.5 kg m^{-3}, but a clear sequence of regions of high and low spice variability cannot be seen. When the isopycnal emerges in the mixed layer, between 28.8° and 31.5°N, spice variability increases and spectral levels tend to peak in the same locations at all wavelengths. North of 31.5°N, water of density 24.8 kg m^{-3} is no longer present and the SeaSoar is towed along the 50 dbar surface. The changes in the wavelet scalogram reflect the changes in the processes that create thermohaline anomalies. At the base of the mixed layer the velocity field is partly across isopycnals because of strong ageostrophic currents, and diapycnal mixing is strong. As a result, the spice scalogram along 24.8 kg m^{-3} is not as stripy as that along 25.5 kg m^{-3}. Spectral levels of spice are higher when the isopycnal is in the mixed layer than when it descends in the thermocline, which can be interpreted as evidence that spice is consumed by mixing processes acting on temperature and salinity patterns as the isopycnal penetrate in the thermocline. The scalogram of spice is more energetic and less stripy along the 24.8 kg m^{-3} isopycnal in the mixed layer than along the 50 dbar isobar. Some of the variability observed along 24.8 kg m^{-3} is probably introduced by the erratic path followed by the SeaSoar in the attempt to track the poorly defined isopycnal in the mixed layer.

5. Depth and Density Dependence of Thermohaline Variability in the Upper Ocean

Data from the 50 and 200 dbar tows demonstrate that thermohaline gradients are strongly coherent over horizontal scales larger than 20 m. In the mixed layer, temperature and salinity gradients are correlated so that they tend to compensate in their effect on density. In the upper thermocline, density gradients due to temperature are twice as large but opposite to those due to salinity. The goal of this section is to use data collected along a sawtooth pattern to study how the T-S relationship changes with depth between the surface and 320 m.

The data collected by profiling along a sawtooth pattern are averaged into bins of 12 min in time (equivalent to a horizontal resolution of ~ 3 km) by 8 m in depth as discussed in section 2. A diagram of potential temperature versus salinity for all binned data shows that thermohaline variability is mostly along isopycnals in the mixed layer and develops a diapycnal component only at depth (Plate 12). The density–compensated variability observed in the upper 100 m of the ocean is reduced at depth, as proved by the reduced spreading of points along denser isopycnals.

The visual description of compensation offered by Plate 12 can be quantified in terms of spice variance along different isopycnals. Temperature and salinity data are binned in a two-dimensional array of 12 min in time by 0.05 kg m^{-3} in density. Spice variance is

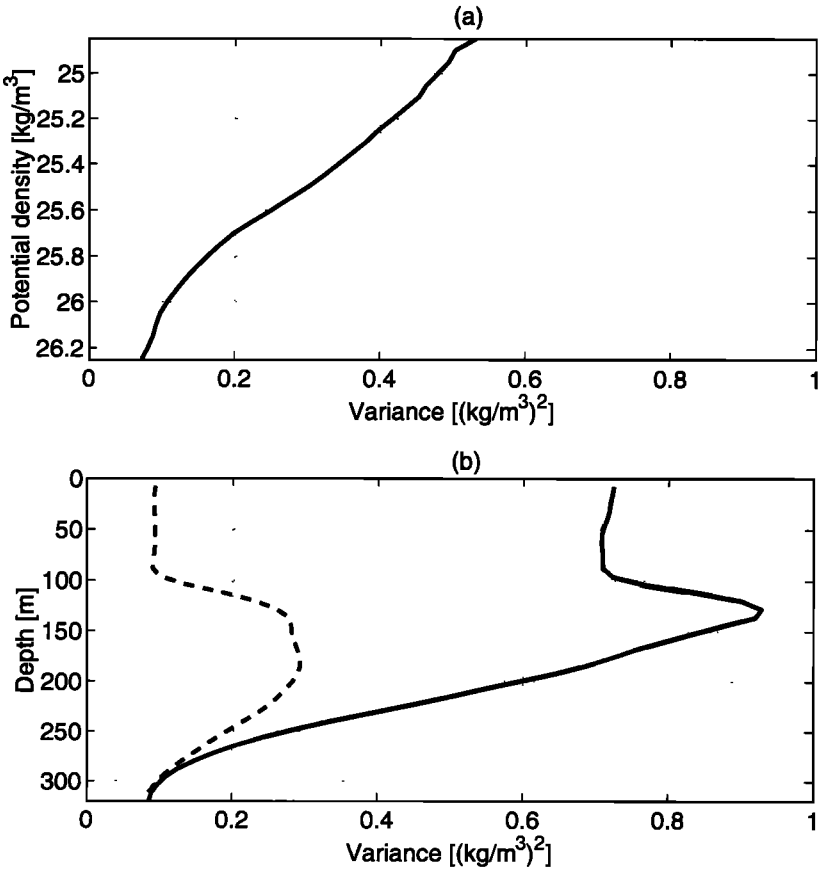

Figure 7. (a) Spice variance along each potential density surface that spans the whole range of 10° in latitude. (b) Spice variance (solid line) and potential density variance (dashed line) as a function of depth. As a function of density, spice variability decreases along deeper isopycnals, while as a function of depth, it reaches its maximum at depths crossed by the base of the mixed layer. Density variance is smaller than spice variance at all depths.

computed separately for each density bin as

$$\sigma_\tau^2 = \left\langle \left[\alpha(\theta - \langle\theta\rangle) + \beta(S - \langle S\rangle) \right]^2 \right\rangle,$$

where averages are carried over all points in a density class and the expansion coefficients α and β are computed for the average temperature and salinity. Spice variance decreases monotonically as a function of density (Figure 7a). Isopycnals that either outcrop at the surface or sink below 320 m are omitted from Figure 7a, because a comparison of total variance is meaningful only for surfaces that span the same latitude range. A reduction of spice variability with increasing density is expected because denser isopycnals are subducted by the wind-driven circulation at higher latitudes [*Talley*, 1985] and have experienced dissipation for a longer time.

Spice variance computed from data gridded as a function of depth does not decrease monotonically with depth (Figure 7b). The largest spice variability is in the depth range occupied by the base of the mixed layer, between 100 and 150 m, where both temperature and salinity change abruptly. Spice variance is larger along isobars than along isopycnals because horizontal profiles include both along-isopycnal and diapycnal variability when surfaces of constant density are tilted. Further insight is gained by comparing spice and potential density variance as a function of depth. Spice variance is much larger than potential density variance in the upper 250 m of the water column because salinity opposes temperature gradients (Figure 7b). At depth, spice and density variances become comparable. The deeper portion of the sawtooth profile is below the surface salinity maximum, and there salinity stratification is too weak to contrast temperature.

The degree of thermohaline compensation can be quantified by computing the density ratio from data gridded as a function of depth. Wavelet coefficients of temperature and salinity are calculated at a wavelength of 10 km, separately for each depth, using a Morlet mother wavelet with $Q = \sqrt{2}\pi$. The horizontal spacing of the gridded data is 3 km, and a small Q is necessary to resolve properly the wiggles of the wavelet over 10 km. The two measures of density ratio, median R and slope of the principal axis, help to understand how the T-S relation varies with depth. Both measures estimate a

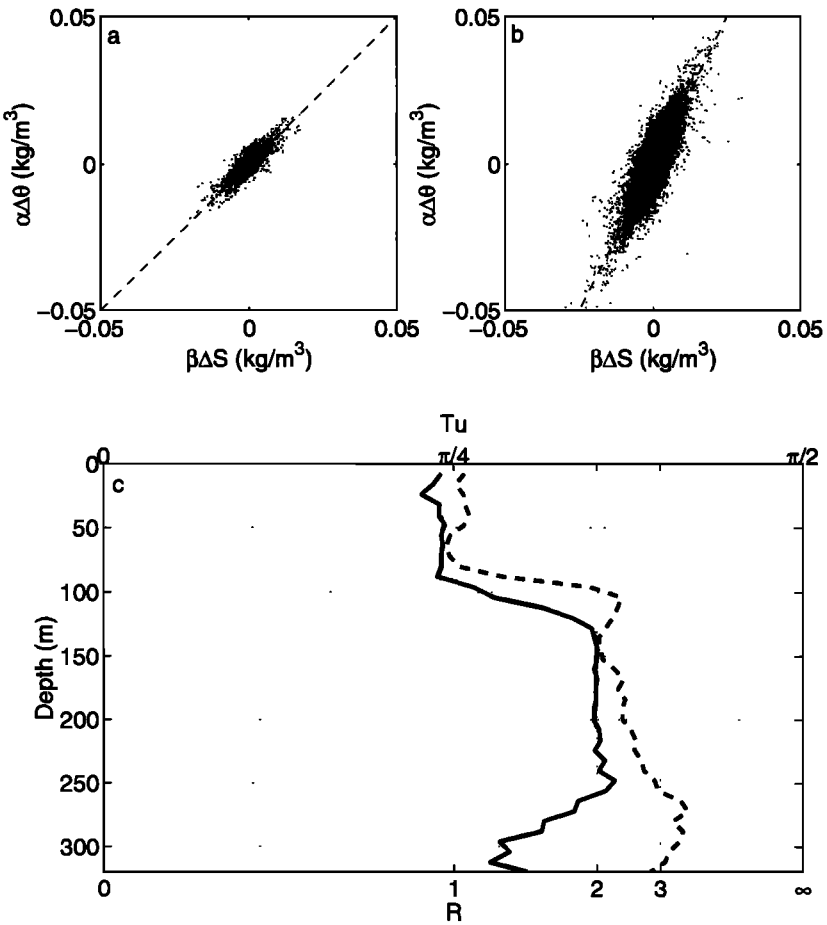

Figure 8. Horizontal density ratio as a function of depth computed from data collected profiling along a sawtooth pattern between the surface and 320 m. (c) The density ratio, estimated as the median R (solid line) and as the slope of the principal axis (dashed line) of wavelet coefficients for a wavelength of 10 km. To emphasize the sharp change in density ratio across the base of the mixed layer, scatterplots of the wavelet coefficients of potential temperature and salinity, each multiplied by the respective expansion coefficients, are shown separately for measurements (a) in the mixed layer and (b) in the thermocline. The mixed layer base is defined by a 0.1 kg m^{-3} difference from the shallowest measurement. Scatter plots are elongated along a line of slope 1 in the mixed layer (dashed line), indicating a tendency for compensation. In the thermocline the scatterplots are tilted along a steeper line in agreement with a density ratio close to 2, shown as a dashed line of slope 2.

density ratio of 1 in the mixed layer and between 2 and 3 in the upper thermocline (Figure 8c). The sharp transition between the two values happens across the base of the mixed layer, which spans the depth range between 100 and 150 m (Plate 1). Scatterplots of the wavelet coefficients of temperature and salinity separately for measurements above and below the mixed layer emphasize how abrupt the transition between the two water masses is (the base of the mixed layer is defined by a 0.1 kg m^{-3} density difference from the shallowest measurement). The points in the scatterplots are close to a slope of 1 in the mixed layer and tilted at a steeper angle in the thermocline (Figures 8a and 8b). Despite exchanges of waters by entrainment and detrainment between the mixed layer and the thermocline the T-S structure in the two layers is very different.

The increase of density ratio with depth is sharper in the slope of the principal axis than in the median R. In the range of depths between 100 and 150 m the horizontal thermohaline gradients are a combination of two different populations: compensated fronts in the mixed layer and the horizontal projection of diapycnal fronts in the upper thermocline. The slope of the principal axis is extremely sensitive to the large diapycnal gradients, and its value shifts to 2 at 100 m in response to a few sub-mixed-layer gradients. The median R increases gradually from 1 to 2 in the 100-150 m range, as the fraction of thermohaline gradients sampled from the thermocline grows and eventually outnumbers the mixed layer gradients. For depths between 150 and 250 m the slope of the principal axis is slightly larger than the median R because north of 32.5°N the stratification is weak, and

haline gradients are not as well correlated with temperature fluctuations; these weak density fronts reduce the median but do not affect the principal axis. Below 250 m the two estimators drift apart because they respond differently to the weak salinity stratification at depth.

The density ratio evolves from 1 to 2 across the base of the mixed layer, and spice is reduced along deeper isopycnals. This does not imply that the T-S relationship is any tighter in the thermocline than in the mixed layer. The opposite is actually true. In the mixed layer the T-S diagram is collapsed along an isopycnal, while at depth the T-S points are quite spread but the thermohaline variability along isopycnals is reduced.

6. Discussion and Conclusions

The Spice experiment has revealed the thermohaline structure of the upper ocean on a wide range of scales. Measurements along the 50 dbar isobar in the mixed layer show that temperature and salinity gradients on horizontal scales of 20 m to 10 km tend to compensate in their effect on density. This result contrasts with the structure measured at 200 dbar in the upper thermocline on the same range of scales where density differences due to temperature are correlated with but exceed density differences due to salinity by a factor of ~ 2. A sawtooth profile shows that the horizontal density ratio increases rapidly from 1 to 2 across the base of the mixed layer. Small–scale temperature and salinity gradients cluster around large–scale thermohaline fronts in the mixed layer along isobars and in the thermocline along isopycnals. The distribution of thermohaline variability in the seasonal thermocline is different along isobars and isopycnals. Along isobars it is dominated by internal waves; along isopycnals it is dominated by geostrophic stirring. Spice variability is reduced along deeper isopycnals.

In the mixed layer, horizontal temperature and salinity fronts tend to be compensated at all scales from tens of meters to tens of kilometers. This can be rationalized in terms of simple dynamics. Random atmospheric forcing and entrainment of thermocline waters introduce horizontal temperature and salinity gradients in the mixed layer. The subsequent slumping of the heavy fluid under light fluid together with vertical mixing removes any horizontal density differences while leaving behind those temperature and salinity differences that do not affect density. A horizontal diffusivity dependent on the density gradient reproduces this behavior [*Ferrari and Young,* 1997], but the specific functional dependence cannot be inferred from the measurements. The mixing of horizontal density gradients is so efficient that only its end consequences are typically observed.

An important question is whether the compensation seen in the mixed layer of the North Pacific subtropical gyre is representative of other oceans. Observations reveal that temperature and salinity balance in their joint effect on density at all scales smaller than 10 km, roughly the local Rossby radius of deformation computed across the base of the mixed layer. At these scales the thermohaline structure is likely to be independent of geographical location. Analysis of SeaSoar data from the Subduction experiment in the winter mixed layer of the subtropical North Atlantic confirms that T-S fronts are typically compensated on the horizontal scales of a few kilometers resolved in this experiment [*Rudnick and Luyten,* 1996]. Compensation is therefore to be expected in all mixed layers if vertical mixing is strong enough to mix away slumping isopycnals, as in midlatitudes during winter. The horizontal structure of mixed layers in other seasons, when mixing is weak, might be substantially different. Finally, the small density changes on scales larger than 10 km are likely to be special to the region of the North Pacific under consideration. *Hautala and Roemmich* [1998] find that the waters subducted from the surface mixed layer sampled in the Spice experiment form a thick layer of constant density at depth.

The present analysis shows that the mixed layer density ratio is typically 1 at scales shorter than 10 km, while *Stommel* [1993] and *Chen* [1995] found that at basin scales the density ratio in the subtropics has a mean close to 2. These results suggest the hypothesis that the density structure of the winter mixed layer is step–like with regions of $R = 1$ separated by sharp density fronts (as observed near the Azores frontal region by *Rudnick and Luyten* [1996]). The large-scale density ratio is then other than unity because it measures a few noncompensated frontal zones, but most of the thermohaline structure is actually compensated. Observational confirmation of the existence of a staircase-like T-S relationship requires horizontal tows long enough to cross a number of strong density fronts.

The question remains as to what sustains a large-scale density ratio of ~ 2 in the world's oceans. External surface forcing is certainly important: the meridional gradient in heat flux dominates that of freshwater flux, driving the large-scale density ratio of the mixed layer toward values larger than 1. However ,the ratio of heat to freshwater fluxes is variable in large-scale maps and does not drive the mixed layer toward a constant density ratio of 2 [*Schmitt et al.,* 1989]. Apparently, the the large-scale density ratio is the result of the combined action of external forcing and internal dynamics of the ocean. An obvious direction of future research is to extend the nonlinear diffusion models discussed by *Ferrari and Young* [1997] to include atmospheric forcing. The presence of atmospheric feedbacks on thermal anomalies, but not salinity ones, might break the symmetry between T and S at large scales, as proposed by *Stommel* [1993] in his "mixed layer regulator" model, and produce a step–like mixed layer formed of compensated T-S gradients separated by a few localized density fronts.

The external forcing on the mixed layer is due to me-

chanical stirring as well as buoyancy fluxes. The effect of stirring on distributions of temperature and salinity is investigated using the wavelet transform. Wavelet scalograms show that small-scale variability of spice peaks around large-scale thermohaline fronts. Colocation of fronts at large and small scales is interpreted as evidence that the velocity field cascades spatial variability from large to small scales [*Klein and Hua,* 1990]. The T-S structure of the mixed layer is therefore the result of various processes. Surface buoyancy fluxes and entrainment of thermocline waters create horizontal thermohaline anomalies. Stirring by geostrophic and wind-driven velocity fields creates temperature and salinity gradients at small scales. The combined action of slumping and mixing rapidly destroys density gradients at small scales.

Tows along 200 dbar and along a sawtooth profile demonstrate that the diapycnal density ratio in the waters below the mixed layer is close to 2. There are two conceivable explanations for the density ratio of 2 in the upper thermocline. The first is that the density ratio of 2 is set in the thermocline by double diffusion [*Schmitt,* 1981, 1994, 1999]. The second is that the large-scale density ratio of 2 in the mixed layer is transferred at depth as waters are subducted. Both mechanisms are likely to play a role and deserve attention. The double-diffusive process of salt fingering is particularly active when the density ratio is near 1 but is ineffective at density ratios above 2. In the thermocline low levels of turbulence [*Gregg,* 1989; *Ledwell et al.,* 1993] allow double diffusion to develop, and the density ratio of 1 is progressively modified as the mixed layer waters are subducted until a value of 2 is reached. In addition, *Stern* [1967] showed that fingering instability is a strong spice consumer. Salt fingers cause warm salty anomalies to rise across isopycnals, because they lose more salt than heat, and cold fresh anomalies to sink across isopycnals, because they gain more salt than heat. The process continues until the anomalies disappear and spice is eliminated.

The alternative explanation of the T-S relation in the upper thermocline starts from the observation that the thermocline waters measured in the Spice experiment have been recently subducted by the wind–driven convergence of mixed layer waters at midlatitudes [*Talley,* 1985]. Therefore *Stommel*'s [1993] observation that the large scale density ratio is $\sim$2 in the mixed layer of all subtropical oceans together with *Iselin*'s [1939] result that vertical profiles of temperature and salinity in the subtropical thermocline are coincident with meridional profiles in the winter mixed layer suggest that the diapycnal structure of the mixed layer is transferred unaltered at depth. In the thermocline, geostrophic currents tend to follow isopycnals, and they stir those portions of the temperature and salinity fields that are compensated. The large spice gradients produced by stirring are eventually destroyed by mixing, leaving behind only the noncompensated T-S gradients [*Stommel,* 1962]. Measurements along a sawtooth profile showed that spice is indeed reduced along deeper isopycnals, which are subducted farther north from the region sampled and have experienced geostrophic stirring for a longer time.

The results of the Spice experiment raise some interesting issues for numerical modeling of the upper ocean. The density–driven mixing active in the winter mixed layer is the result of isopycnal slumping and vertical mixing on scales of 100 m, but it creates compensation on scales of 10 km. There are ocean circulation models that can resolve scales of 10 km. If some parameterization of density–driven mixing is not included in these models, the horizontal structure of the mixed layer will resemble the atmospheric forcing and will not be characterized by density–compensated structures. Further, any inaccuracy in the horizontal structure of the mixed layer is transported at depth along isopycnals and affects the overall T-S relation of the subtropical thermoclines.

Appendix A: Calibration of the Sensors

The Sea-Bird CTD probes measure temperature T and electrical conductivity C of seawater. Meaningful small-scale salinity measurements require temperature and conductivity sensors that are colocated and whose frequency response are matched over the scales of interest. The consequences of not meeting these conditions are seen at regions of high gradients in temperature and conductivity because artificially high or low values of salinity and density can appear in the measurements. This phenomenon is referred to as salinity spiking. Digital filters are applied to the time series to correct for the mismatch caused by the difference in the sensor responses and by the phase lag due to the physical separation of the sensors along the tow direction.

The simplest model includes a time lag between conductivity and temperature and an exponential relaxation of temperature to its true value [*Horne and Toole,* 1980]. In mathematical terms a set of two partial differential equations relates the temperature T and conductivity C of a water parcel to the measured T_{obs} and C_{obs} at time t,

$$T(t) = \tau_T \frac{dT_{obs}(t)}{dt} + T_{obs}(t) \qquad \text{(A1)}$$

$$C(t) = C_{obs}(t + \tau_C), \qquad \text{(A2)}$$

and in Fourier space,

$$\widehat{T}(f) = (1 - 2\pi i f \tau_T)\widehat{T}_{obs}(f) \qquad \text{(A3)}$$

$$\widehat{C}(f) = \exp(-2\pi i f \tau_C)\widehat{C}_{obs}(f). \qquad \text{(A4)}$$

$\widehat{T}(f)$ and $\widehat{T}_{obs}(f)$ are the Fourier transforms of the true and the observed temperature profiles, $\widehat{C}(f)$ and $\widehat{C}_{obs}(f)$ are the Fourier transforms of the true and the observed conductivity profiles, and f is frequency. Equations (A1)-(A4) provide a relationship between the

true and observed spectra and are used to calibrate the measurements.

In order to obtain τ_T and τ_C, the conductivity of seawater is assumed to be linearly related to temperature, with a much smaller dependence on salinity, pressure, and higher-order temperature terms. The cross-spectrum between T_{obs} and C_{obs} can therefore be approximated by

$$\left\langle \widehat{T}^*_{obs}(f)\widehat{C}_{obs}(f)\right\rangle = \gamma\frac{\exp(2\pi i f\tau_C)}{1+2\pi i f\tau_T}\left\langle \left|\widehat{T}(f)\right|^2\right\rangle, \quad \text{(A5)}$$

where $\gamma = \partial C/\partial T$ and $\langle\,\rangle$ denotes an ensemble average. The constants τ_T and τ_C are determined by fitting the function $2\pi f\tau_C - \arctan(2\pi f\tau_T)$ to the phase of the observed cross-spectrum. The fit is done using only frequencies below 4 Hz because the signal becomes too noisy at higher frequencies. The values obtained are $\tau_T = 0.05$ s and $\tau_C = 0.02$ s along the sawtooth tow and $\tau_T = 0.08$ s and $\tau_C = 0.01$ s along the isobar and isopycnal tows. The change in the time response of the sensors is a consequence of the different properties of the flow during the various tows. True temperature and conductivity spectra are reconstructed by applying the filters $(1-2\pi i f\tau_T)$ and $\exp(-2\pi i f\tau_C)$ to the Fourier transforms of T_{obs} and C_{obs} low passed at 4 Hz. The corrected temperature and salinity signals are finally averaged in 1 s bins to obtain stable measurements. A temporal resolution of 1 s corresponds to a spatial resolution of 4 m at the cruising velocity of 4 m s^{-1}.

No correction is made for the effect of thermal mass in the response of the conductivity cell. *Morison et al.* [1994] found that thermal mass can cause an offset between T-S curves for upward and downward casts. This symptom is not seen in the data set analyzed here. In fact the towing speed (and therefore the flushing rate) is 4 m s^{-1} and the vertical profiling speed is typically 1 m s^{-1} in the sawtooth tow, and substantially less in the isobar and isopycnal tows, and therefore thermal mass effects are expected to be smaller than in the study referenced, where vertical velocities were substantially higher.

Appendix B: The Wavelet Transform

Frequently in oceanography integral transforms are used to relate a signal $f(x)$ to a basis of analyzing functions $\psi_a(x)$,

$$\widetilde{f}(a,x) = \int_{-\infty}^{+\infty} f(x')\psi^*_a(x'-x)dx'. \quad \text{(B1)}$$

The function $\widetilde{f}(a,x)$ is called the transform of $f(x)$ and it is a function of the parameter a, involved in the definition of the basis ψ_a. Using the convolution theorem, the integral transform (B1) can be equivalently written is terms of the Fourier transforms $\widehat{f}(k)$ of $f(x)$ and $\widehat{\psi}_a(k)$ of $\psi_a(x)$,

$$\widetilde{f}(a,x) = \frac{1}{2\pi}\int_{-\infty}^{+\infty} \widehat{f}(k)\widehat{\psi}^*_a(k)\exp(-i\,k\,x)dk. \quad \text{(B2)}$$

The intervals Δx and Δk, over which the integrands in (B1) and (B2) are significantly different from zero, are always such that the product $\Delta x \cdot \Delta k$ is bounded from below (the value of this lower limit depends on the exact definitions of Δx and Δk). This result is known as the *Heisenberg uncertainty principle* in quantum physics. The wavelet transform achieves a good compromise for compactness in location and wavenumber with a basis of analyzing functions in the form of wave packets with a finite spread in both spaces [*Daubechies,* 1992; *Farge,* 1992; *Holschneider,* 1995]. The tradeoff between compactness in x and k spaces is chosen to maintain the same resolution (number of oscillations of the analyzing function in Δx) at all wavenumbers. That is, the wavelength of the oscillation increases proportionally to the localization in space Δx so that the analyzing functions maintain a constant number of oscillations for all k.

In mathematical terms the continuous wavelet transform of a signal $f(x)$ is defined as the integral transform with a family of analyzing functions $\psi_{l,x_0}(x) = A(l)\psi\left(\frac{x-x_0}{l}\right)$ and is given by the set of coefficients

$$\widetilde{f}(l,x_0) = \int_{-\infty}^{+\infty} f(x)\psi^*_{l,x_0}(x)dx, \quad \text{(B3)}$$

where l is the scale parameter and x_0 is the location parameter. The functions $\psi_{l,x_0}(x)$ are called wavelets. Changing the value of l has the effect of dilating ($|l| > 1$) or contracting ($|l| < 1$) the function $\psi(x)$. Changing x_0 has the effect of analyzing the signal $f(x)$ at different positions. The normalization factor $A(l)$ is arbitrary: in this paper it is either $1/|l|$ or $1/\sqrt{|l|}$. The first choice is used in the analysis of the density ratio and guarantees that the wavelet transform has unit gain. The second choice is used to compute scalograms and ensures that the integral of the wavelet transform in wavelength and location gives the total energy.

The function $\psi(x)$, called the *mother wavelet,* must satisfy two requirements: (1) it must be compact in location and wavenumber space; that is, Δx and Δk must be finite, and (2) it must satisfy the admissibility condition

$$C_\psi = \frac{1}{2\pi}\int_{-\infty}^{+\infty}\frac{\left|\widehat{\psi}(k)\right|^2}{|k|}dk < \infty. \quad \text{(B4)}$$

Condition (1) implies that the spread of the mother wavelet in x space must be finite ($\Delta x = \sigma < \infty$) and proportional to the spread in k space ($\Delta k = D/\sigma$ for some constant D). The localization of the wavelet $\psi_{l,x_0}(x)$ in x space is then $l\sigma$ and in k space it is $D/l\sigma$. Condition (2) guarantees that $\widehat{\psi}(k)$ decays rapidly as $k \to \infty$ and that $\widehat{\psi}(0) = 0$. The mother wavelet has therefore zero mean, $\int_{-\infty}^{+\infty}\psi(x)dx = 0$.

If Δx and Δk are defined as the square roots of the second moments of $|\psi|^2$ in the x and k spaces, the mother wavelet that minimizes the product $\Delta x \cdot \Delta k$ is the so-called Morlet mother wavelet,

$$\psi(x) = (\pi)^{-1/2} \exp(-x^2) \exp(iQx). \qquad \text{(B5)}$$

This mother wavelet does not satisfy the admissibility condition because $\widehat{\psi}(0) \neq 0$, but for $|Q| > 4$ the Morlet wavelet at zero wavenumber is not different from zero for calculations in single precision. The resolution of the Morlet wavelet is set by the quality factor Q, i.e. the ratio of the wavenumber at which the window is centered to its spread in the k space.

Acknowledgments. We would like to thank William Young for useful discussions. We are grateful to the members of the SIO SeaSoar group, Lloyd Regier, Lyn Harris, and John Paoli, for their hard work during the various stages of the Spice experiment. The willing assistance of Captain Murline and the crew of the R/V *New Horizon* is appreciated. This work was supported by National Science Foundation grant OCE95-29752.

References

Batchelor, G. K., Small scale variation of convected quantities like temperature in turbulent fluid, Part 1, *J. Fluid. Mech., 5*, 113-134, 1959.

Chen, L. G., Mixed layer density ratio from the Levitus data, *J. Phys. Oceanogr., 25*, 691-701, 1995.

Danaila, L., P. Le Gal, F. Anselmet, F. Plaza, and J. F. Pinton, Some new features of the passive scalar mixing in a turbulent flow, *Phys. Fluids, 11*, 636-645, 1999.

Daubechies, I., *Ten Lectures on Wavelets, CBMS-NSF Reg. Conf. Ser. Appl. Math.*, 357 pp., Soc. for Ind. and Appl. Math., Philadelphia, Pa., 1992.

Dugan, J. P., B. W. Stalcup, and R. L. DiMarco, Statistics of small-scale activity in the upper ocean, *J. Geophys. Res., 97*, 5665-5675, 1992.

Efron, B., *The Jackknife, the Bootstrap and Other Resampling Plans*, 92 pp., Soc. for Ind. and Appl. Math., Philadelphia, Pa., 1982.

Farge, M., Wavelet transforms and their application to turbulence, *Annu. Rev. Fluid Mech., 2*, 395-457, 1992.

Ferrari, R., and W. R. Young, On the development of thermohaline correlations as a result of nonlinear diffusive parameterizations, *J. Mar. Res., 55*, 1069-1101, 1997.

Flament, P., L. Armi, and L. Washburn, The evolving structure of an upwelling filament, *J. Geophys. Res., 90*, 11,765-11,778, 1985.

Gargett, A. E., and R. W. Schmitt, Observations of salt fingers in the central waters of the eastern North Pacific, *J. Geophys. Res., 87*, 8017-8029, 1982.

Garrett, C J. R., and W. H. Munk, Space-times scales of internal waves: A progress report, *J. Geophys. Res., 80*, 291-297, 1975.

Gregg, M. C., Scaling turbulent dissipation in the thermocline, *J. Geophys. Res., 94*, 9686-9698, 1989.

Haine, T. W. N., and J. Marshall, Gravitational, symmetric, and baroclinic instability of the ocean mixed layer, *J. Phys. Oceanogr., 28*, 634-658, 1998.

Hautala, S. L., and D. H. Roemmich, Subtropical mode water in the northeast Pacific Basin, *J. Geophys. Res., 103*, 13,055-13,066, 1998.

Holschneider, M., *Wavelets: An Analysis Tool*, 423 pp., Clarendon, Oxford, England, U. K., 1995.

Horne, E. P. W., and J. M. Toole, Sensor response mismatches and lag correction techniques for temperature-salinity profilers, *J. Phys. Oceanogr., 10*, 1122-1130, 1980.

Iselin, C. O. D., The influence of vertical and lateral turbulence on the characteristics of waters at mid-depth, *EOS Trans. AGU, 20*, 414-417, 1939.

Jackett, D. R., and T. J. McDougall, An oceanographic variable for the characterization of intrusions and water masses, *Deep Sea Res. Part A., 32*, 1195-1207, 1985.

Klein, P., and B. L. Hua, The mesoscale variability of the sea surface temperature: An analytical and numerical model, *J. Mar. Res., 48*, 729-763, 1990.

Ledwell, J. R., A. J. Watson, and C. S. Law, Evidence for slow mixing across the pycnocline from an open-ocean tracer-release experiment, *Nature, 364*, 701-703, 1993.

Mack, S. A., Towed-chain measurements of ocean microstructure, *J. Phys. Oceanogr., 19*, 1108-1129, 1989.

Mack, S. A., and H. C. Schoeberlein, Discriminating salt fingering from turbulence-induced microstructure: Analysis of towed temperature-conductivity data, *J. Phys. Oceanogr., 23*, 2073-2106, 1993.

Magnell, B., Salt fingers observed in the Mediterranean Outflow region (34°N, 11°W) using a towed sensor, *J. Phys. Oceanogr., 6*, 511-523, 1976.

Morison, J. R., N. Andersen, N. Larson, E. D'Asaro, and T. Boyd, The correction for thermal-lag effects in Sea-Bird CTD data, *J. Atmos. Oceanic Technol., 11*, 1151-1164, 1994.

Munk, W., Internal waves and small scale processes, in *Evolution of Physical Oceanography: Scientific Surveys in Honor of Henry Stommel*, edited by B. A. Warren and C. Wunsch, pp. 264-291, MIT Press, Cambridge, Mass., 1981.

Pavan, V., and I. M. Held, The diffusive approximation for eddy fluxes in baroclinically unstable jets, *J. Atmos. Sci., 53*, 1262-1272, 1996.

Roden, G. I., On north Pacific temperature, salinity, sound velocity and density fronts and their relation to the wind and energy flux fields, *J. Phys. Oceanogr., 5*, 557-571, 1975.

Roden, G. I., The vertical thermohaline structure in the Argentine Basin, *J. Geophys. Res., 94*, 877-896, 1989.

Rudnick, D. L., and R. Ferrari, Compensation of horizontal temperature and salinity gradients in the ocean mixed layer, *Science, 283*, 526-529, 1999.

Rudnick, D. L., and J. R. Luyten, Intensive survey of the Azores Front, 1, Tracers and dynamics, *J. Geophys. Res., 101*, 923-939, 1996.

Samelson, R. M., and C. A. Paulson, Towed thermistor chain observations of fronts in the subtropical North Pacific, *J. Geophys. Res., 93*, 2237-2246, 1988.

Schmitt, R. W., Form of the temperature-salinity relationship in the central water: Evidence for double-diffusive mixing, *J. Phys. Oceanogr., 11*, 1015-1026, 1981.

Schmitt, R. W., Double diffusion in oceanography, *Annu. Rev. Fluid Mech., 26*, 255-285, 1994.

Schmitt, R. W., Oceanography - Spice and the demon, *Science, 283*, 498-499, 1999.

Schmitt, R. W., and D. L. Evans, An estimate of the vertical mixing due to salt fingers based on observations in the North Atlantic central water, *J. Geophys. Res., 83*, 2913-2919, 1978.

Schmitt, R. W., P. S. Bodgen, and C. E. Dorman, Evaporation minus precipitation and density fluxes for the North Atlantic, *J. Phys. Oceanogr., 9*, 1208-1221, 1989.

Shinskey, F. G. *Processes Control Systems: Application, Design, Adjustment*, McGraw-Hill, New York, 1988.

Sinai, Y. G., and V. Yakhot, Limiting probability distributions of a passive scalar in a random velocity field, *Phys. Rev. Lett.*, *63*, 1962-1964, 1989.

Stern, M. E., Lateral mixing of water masses, *Deep Sea Res. Oceanogr. Abstr.*, *14*, 747-753, 1967.

Stommel, H., Thermohaline convection with two stable regimes of flow, *Tellus*, *13*, 224-230, 1961.

Stommel, H., On the cause of the temperature-salinity curve in the ocean, *Proc. Natl. Acad. Sci. U.S.A.*, *48*, 764-766, 1962.

Stommel, H., A conjectural mechanism for determining the thermohaline structure of the oceanic mixed layer, *J. Phys. Oceanogr.*, *23*, 142-158, 1993.

Stommel, H. M., and W. R. Young, The average T-S relation of a stochastically forced box model, *J. Phys. Oceanogr.*, *23*, 151-158, 1993.

Talley, L. D., Ventilation of the subtropical North Pacific: The shallow salinity minimum, *J. Phys. Oceanogr.*, *15*, 633-649, 1985.

Veronis, G., On properties of seawater defined by temperature, salinity and pressure, *J. Mar. Res.*, *30*, 227-255, 1972.

Visbeck, M., J. Marshall, T. Haine and M. Spall, Specification of eddy transfer coefficients in coarse-resolution ocean circulation models, *J. Phys. Oceanogr.*, *27*, 381-402, 1997.

Young, W. R., The subinertial mixed layer approximation, *J. Phys. Oceanogr.*, *24*, 1812-1826, 1994.

Yuan, X., and L. D. Talley, Shallow salinity minima in the North Pacific, *J. Phys. Oceanogr.*, *22*, 1302-1316, 1992.

R. Ferrari and D. L. Rudnick, Scripps Institution of Oceanography, La Jolla, CA 92093-0230. (rferrari@ucsd.edu; drudnick@ucsd.edu)

(Received August 13, 1999; revised February 14, 2000; accepted March 9, 2000.)